Cell Reports
Medicine

Article

Injectable hydrogel with miR-222-engineered extracellular vesicles ameliorates myocardial ischemic reperfusion injury via mechanotransduction

Graphical abstract

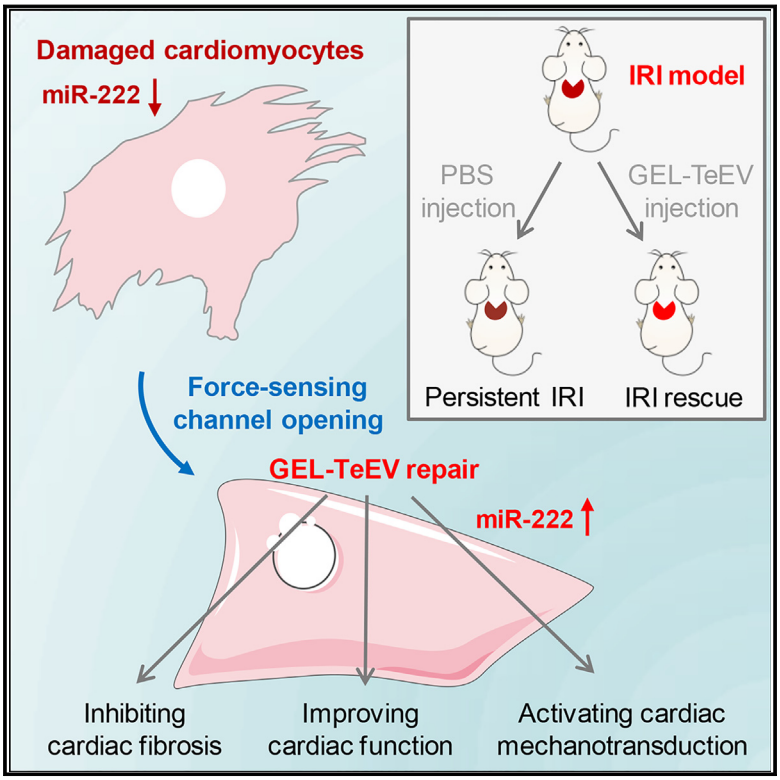

Highlights

- Targeting miR-222-engineered EVs are incorporated in mechanical GEL hydrogels
- GEL-TeEVs are administered into the pericardial cavity by minimally invasive injection
- Mechanical GEL-TeEV patches attenuate cardiac IRI remodeling
- Improvements are linked to adhesion, force, and mechanotransduction preservation

Authors

Yongtao Wang, Danni Meng, Xiaohui Shi, ..., Dragos Cretoiu, Qiulian Zhou, Junjie Xiao

Correspondence

zhouqiulian@shu.edu.cn (Q.Z.), junjiexiao@shu.edu.cn (J.X.)

In brief

Wang et al. construct injectable pericardial hydrogels with targeting miR-222-engineered extracellular vesicles (TeEVs) as biofunctional cardiac patches to ameliorate acute myocardial ischemic reperfusion injury (IRI) and mitigate cardiac remodeling post IRI. Meanwhile, the improvements of cardiac functions are related to focal adhesion activation, cytoskeleton force enhancement, and nuclear force-sensing preservation.

Wang et al., 2025, Cell Reports Medicine 6, 101987
March 18, 2025
https://doi.org/10.1016/j.xcrm.2025.101987

CellPress

Cell Reports Medicine

CellPress
OPEN ACCESS

Article

Injectable hydrogel with miR-222-engineered extracellular vesicles ameliorates myocardial ischemic reperfusion injury via mechanotransduction

Yongtao Wang,[1,2,8] Danni Meng,[1,2,8] Xiaohui Shi,[1,2,8] Yan Hou,[1] Shihui Zang,[1] Lei Chen,[3,4] Michail Spanos,[5] Guoping Li,[5] Dragos Cretoiu,[6,7] Qiulian Zhou,[1,2,*] and Junjie Xiao[1,2,9,*]

[1]Cardiac Regeneration and Ageing Lab, Institute of Geriatrics (Shanghai University), Affiliated Nantong Hospital of Shanghai University (The Sixth People's Hospital of Nantong) and School of Life Science, Shanghai University, Nantong 226011, China
[2]Institute of Cardiovascular Sciences, Shanghai Engineering Research Center of Organ Repair, Joint International Research Laboratory of Biomaterials and Biotechnology in Organ Repair (Ministry of Education), School of Life Science, Shanghai University, Shanghai 200444, China
[3]Department of Spine Surgery, Tongji Hospital, School of Medicine, Tongji University, Shanghai 200065, China
[4]Key Laboratory of Spine and Spinal Cord Injury Repair and Regeneration, Ministry of Education, Department of Spine Surgery, Tongji Hospital, School of Medicine, Tongji University, Shanghai 200065, China
[5]Cardiovascular Division of the Massachusetts General Hospital and Harvard Medical School, Boston, MA 02114, USA
[6]Department of Medical Genetics, Carol Davila University of Medicine and Pharmacy, 020031 Bucharest, Romania
[7]Materno-Fetal Assistance Excellence Unit, Alessandrescu-Rusescu National Institute for Mother and Child Health, 011062 Bucharest, Romania
[8]These authors contributed equally
[9]Lead contact
*Correspondence: zhouqiulian@shu.edu.cn (Q.Z.), junjiexiao@shu.edu.cn (J.X.)
https://doi.org/10.1016/j.xcrm.2025.101987

SUMMARY

Cardiac ischemic reperfusion injury (IRI) significantly exacerbates cardiac dysfunction and heart failure, causing high mortality. Despite the severity of IRI, effective therapeutic strategies remain elusive. Acellular cardiac patches have shown considerable efficacy in delivering therapeutics directly to cardiac tissues. Herein, we develop injectable GelMA (GEL) hydrogels with controlled mechanical properties. Targeting miR-222-engineered extracellular vesicles (TeEVs), tailored with cardiac-ischemia-targeting peptides (CTPs), are developed as ischemic TeEV therapeutics. These TeEVs are encapsulated within mechanical hydrogels to create injectable TeEV-loaded cardiac patches, enabling minimal invasiveness to attenuate IRI. The injectable patches facilitate the precise targeting of TeEVs for the efficient rescue of damaged cells. Persistent delivery of TeEVs into the infarcted region alleviates acute IRI and mitigated remodeling post IRI. This is linked to focal adhesion activation, cytoskeleton force enhancement, and nuclear force-sensing preservation. These findings may pave the way for force-sensing approaches to cardiac therapy using bioengineered therapeutic patches.

INTRODUCTION

Cardiovascular diseases (CVDs) remain the leading cause of fatality worldwide.[1] Even though patients with CVD may achieve remission through temporary conservative and surgical therapies, the re-hospitalization and mortality rates remain high.[2,3] Various heart diseases, including acute myocardial infarction (MI) and heart failure (HF), continue to pose a significant risk to human lives, becoming a major public health concern globally.[4–6] Regenerative heart therapy, which employs biocompatible materials and biological textures in combination with nucleic acids, proteins, and live cells, is considered as a promising approach to provide personalized precision therapy for severe cardiac ischemic reperfusion injury (IRI) and HF.[7,8] Mechanical hydrogel-based acellular patches are created to passively suppress ischemic infarction regions of the myocardium under force-sensing mechanotransduction, reducing myocardial wall stress and preventing left ventricular dysfunction remodeling.[9] Fluid-like waxy starch hydrogels near the gel point, designed as gel-point adhesion patches, offer appropriate force protection for cardiac injury.[10] Although biofunctional hydrogels are widely implemented for cardiac regeneration and repair, minimal manipulation by injectable hydrogels holds potential for treating CVDs through force-sensing mechanical protection.

Ischemia and hypoxia of the coronary arteries cause the loss of cardiomyocytes, finally leading to MI development.[11] Clinically, thrombolysis, percutaneous coronary intervention, and grafting can restore ischemic perfusion of the coronary artery.[12] However, once perfusion occurs, pressure overload (Piezo1-related calcium influx) and high reactive oxygen species cause secondary damage to cardiomyocytes due to the loss of mechanical protection in the cardiac microenvironment.[13–15] Notably, IRI is

closely associated with the cardiomyocyte microenvironment and extracellular matrix (ECM) assembly, particularly in ECM remodeling.[16,17] When cardiomyocytes attach to the ECM microenvironment, they produce integrin adhesion-coupling receptors, exhibit various morphological characteristics, alter nanomechanical interactions based on cytoskeleton-mediated reorganization, and transmit these mechanical signals into the nucleus in response to IRI. This process is crucial for maintaining cardiomyocyte metabolism and survival.[18,19] The alteration of geometric topology in cardiomyocytes promotes the reconstruction of cytoskeleton structures (sarcomere), thus affecting cardiac remodeling after IRI.[20] The dynamic homeostasis of cytoskeletal mechanics is disrupted in cardiac IRI.[21,22] Protein-encoding genes in the sarcomere, such as MYBPC3, which encodes myosin-binding protein C (cMyBP-C) in cardiomyocytes and is involved in regulating sarcomere contraction, can mutate and lead to cardiac diseases.[23] Importantly, cMyBP-C offers a different molecular mechanism to explain how mechanical homeostasis is maintained in cardiomyocytes. The expression of force-sensing proteins acts as a mechanical biotransducer, monitoring cardiovascular functions and cardiac diseases.[24,25]

Extracellular vesicles (EVs) secreted from mesenchymal stem cells (MSCs) are nanoscale vesicles approximately 100 nm in diameter, containing proteins, lipids, and RNAs (including microRNAs [miRNAs], long non-coding RNAs [lncRNAs], and circular RNAs [circRNAs]) for cardiac repair.[19,26–29] Platelet membrane-fused circulating EVs enhance targeting uptake ability in human umbilical vein endothelial cells (HUVECs) and inhibit apoptosis in HUVECs and neonatal rat cardiomyocytes (NRCMs), protecting against acute IRI (AIRI) and improving cardiac dysfunction 3 weeks post IRI remodeling.[30] Moreover, MSC-derived EVs are loaded into hydrogels via injection-free spray methods for efficient cardiac disease therapeutics.[31] We previously reported that miR-222 is profiled to promote cardiomyocyte growth and proliferation in exercise model and protect mammalian heart against pathological remodeling.[32] Therefore, understanding the molecular mechanisms of cardiomyocyte nanomechanics in IRI remodeling induced by miR-222-overexpressed EV-loaded cardiac patches is crucial for elucidating the interaction of IRI mechanics and biomaterial-based force therapy. In this study, we synthesized injectable gelatin methacryloyl (GelMA) hydrogels (GEL) by controlling the grafting ratio of methacryloyl groups and established targeting miR-222-engineered EVs (TeEVs) as therapeutics. TeEVs were loaded into hydrogels to construct an injectable TeEV-loaded pericardial hydrogel patch. GEL-TeEV hydrogels were injected into the pericardial cavity via a minimally invasive method to alleviate myocardial IRI through the protection of force-sensing mechanotransduction. This study not only provides insights into delivering targeting-engineered EVs in cardiac IRI tissues with minimal invasiveness but also offers a deep understanding of cell nanomechanics and mechanotransduction in IRI repair.

RESULTS

Generation and feasibility of TeEV-loaded hydrogel patches

Injectable pericardial GEL hydrogel patches, loaded with TeEVs, were constructed through photosensitive curing to achieve minimally invasive delivery for myocardial IRI rescue via force-sensing mechanotransduction (Figure S1A). The viscoelastic hydrogel was initially synthesized by introducing methacryloyl groups into gelatin chains. The grafting percentage of methacryloyl groups was controlled by varying methacrylic anhydride (MAA) concentrations to produce an adjustable mechanical GEL hydrogel precursor (Figure S1B). The grafting conjugation of methacryloyl groups was verified via ^{1}H-NMR analysis (Figure S1C), which showed an increase in the δ values of proton peaks of methacrylate vinyl groups at 5.4 and 5.7 ppm, while the proton peaks of methylene lysine at 2.9 ppm declined for the synthesized GEL precursor. This indicates an increased modification of MAA in the gelatin chains. Fourier transform infrared spectra of gelatin and GEL precursor were also applied to analyze the synthesized GEL (Figure S1D). The GEL spectrum exhibited characteristic peaks of gelatin chains at 3,292 cm^{-1} for O–H and N–H stretching vibrations, at 1,544 cm^{-1} for N–H stretching and C–H bending peaks, and at 1,237 cm^{-1} for C–N stretching and N–H bending peaks. Notably, the characteristic peak at about 1,631 cm^{-1} in the GEL spectrum was identified as the C=C stretching peak of the methacrylate group, indicating successful synthesis of the GEL precursor. Additionally, a photosensitive reagent was incorporated into the synthesized GEL precursor to establish the mechanical hydrogel platform under UV exposure, used in this study (Figure S1E). The formation of GEL hydrogel was confirmed by SEM, which presented a uniform porous topography (Figure S1F) with interconnected pores averaging approximately 100 μm in diameter. The rheology of gelatin and GEL was evaluated by oscillatory dynamic shearing measurement to assess gelatinization ability (Figure S1G), where the storage modulus (G′) and loss modulus (G″) demonstrated that GEL presented excellent gel stability under varied shear rates. These results indicate that MAA was impeccably integrated into the gelatin chains to manufacture injectable, mechanical, and biocompatible GEL hydrogels.

Human umbilical cord MSC-derived EVs (HUC-MSC-derived EVs) were isolated by ultracentrifugation, engineered to overexpress miR-222 by electroporation, and targeted using a cardiac-ischemia-targeting Cys-Ser-Thr-Ser-Met-Leu-Lys-Ala-Cys (CSTSMLKAC) polypeptide to form cardiac TeEVs (Figure S1H). The miR-222-engineered EVs exhibited an overexpression of miR-222 as compared to control EVs (Figure S1I). The creation of distinct EVs was also corroborated by typical EV markers CD63, CD9, Tsg101, and Alix in engineered EVs (Figure S1J). Moreover, Transmission electron microscopy (TEM) was applied to investigate the nanospherical-shaped configuration and size of miR-222-engineered EV and TeEV nanoparticles (Figure 1A). Nanoparticle tracking analysis (NTA) was performed to calculate the physical sizes and average particle sizes of miR-222-engineered EVs and TeEVs, ranging approximately 80–130 nm (Figure 1B). Therefore, these results present that TeEVs were successfully designed by introducing the cardiac-ischemia-targeting polypeptide into miR-222-engineered EVs.

Subsequently, the TeEVs were loaded into GEL hydrogels to assess the mechanical properties, release profile, and biocompatibility of GEL-TeEV hydrogels. Initially, the mechanical properties of GEL and GEL-TeEV hydrogels were measured using force-distance curves obtained by atomic force microscope (AFM)

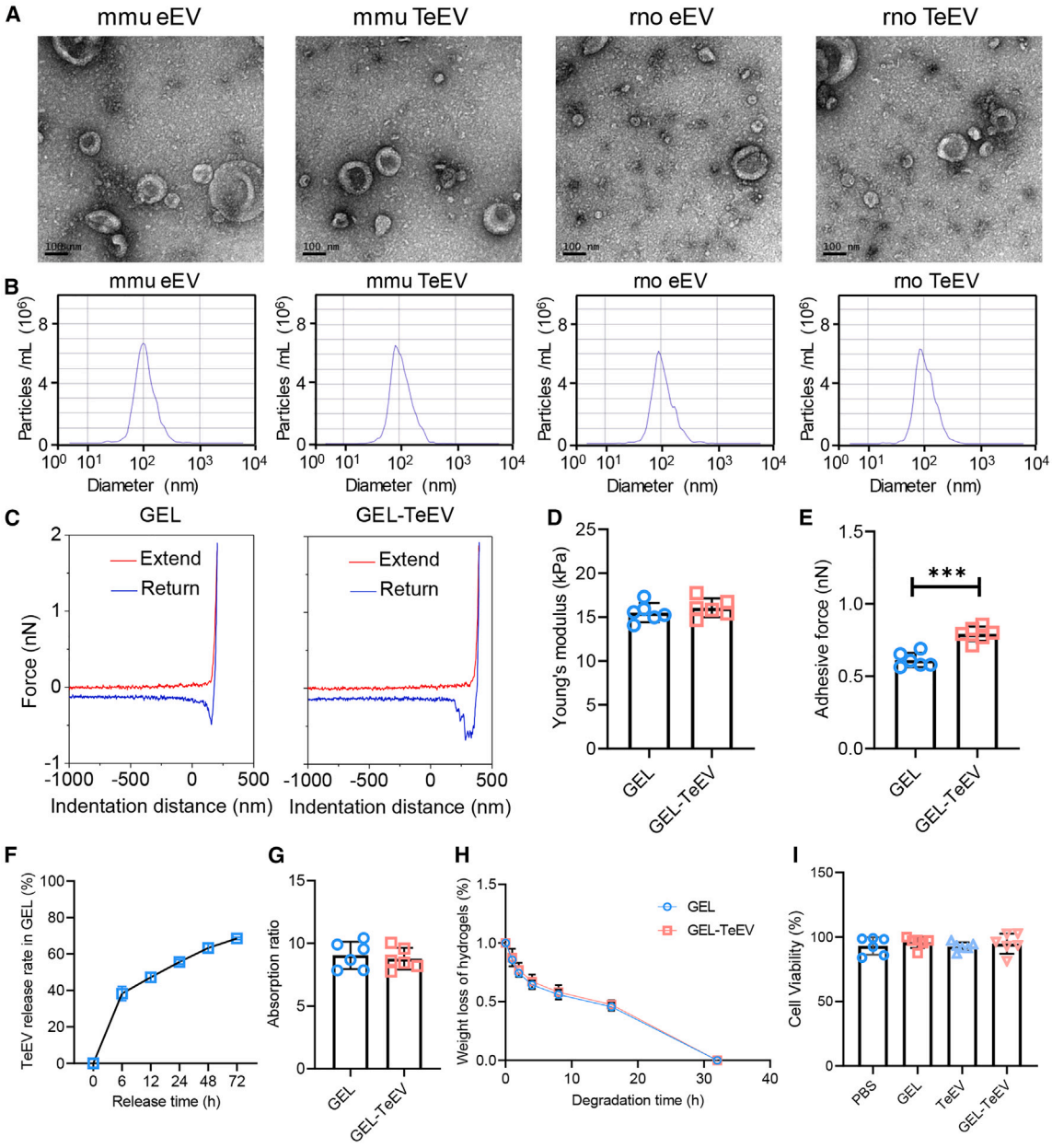

Figure 1. Generation and characterization of targeting miR-222-engineered EVs, mechanical hydrogels (GEL), and TeEV-loaded hydrogel patches (GEL-TeEV)

(A) Representative TEM images of EVs modified by miR-222-engineered and cardiac-ischemia targeting peptides (CTsP) as miR-222-engineered EVs (eEVs) and targeting miR-222-engineered EVs (TeEVs) in both *Mus musculus* (mmu) and *Rattus norvegicus* (rno).

(B) Nanoparticle size distribution of engineered EVs by NTA analysis.

(C) Force-distance curves by AFM measurement.

(D) Young's modulus of GEL and GEL-TeEV.

(E) Adhesive force of GEL and GEL-TeEV.

(F) TeEV release rate in GEL at different time points.

(G) Absorption ratio of mechanical hydrogels.

(H) Degradability evaluated by weight loss of hydrogels.

(I) Cell viability by PBS, GEL, TeEV, and GEL-TeEV treatment.

Data present mean ± SD; $n = 3$ (F) or $n = 6$ per group. Unpaired Student's t test (D–H) and one-way ANOVA test followed by Bonferroni test (I) were used for statistical analysis. ***$p < 0.001$. See also Figure S1.

nanoindentation (Figure 1C). The average Young's modulus of GEL-TeEV samples was calculated to be approximately 14–18 kPa, consistent with GEL samples, indicating that the addition of TeEVs did not affect the crosslinked GEL hydrogels (Figure 1D). Interestingly, the adhesion force of GEL-TeEV samples increased compared to GEL samples (Figure 1E), suggesting that the elevated adhesion force may provide a strong cardiac binding force in heart patch formation. The slow-release performance of TeEVs in GEL was monitored by measuring the TeEV content in the supernatant (Figure 1F). TeEV release profile was enhanced with increasing release time, with approximately 40% of TeEVs released and diluted in supernatant PBS within 6 h, revealing a rapid initial release. Subsequently, TeEV release amount accumulated to 70% within 72 h. The TeEV release profile was closely associated with the absorption ability and degradability of the hydrogel. The absorption assay in PBS and degradability assay in collagenase showed little significant difference in equilibrium absorption ratio (Figure 1G) and weight loss (Figure 1H) of GEL hydrogels with or without TeEV incorporation. In addition, the biocompatibility of the crosslinked hydrogels was evaluated by analyzing cell survival ability in synthesized hydrogels. Cardiomyocytes cultured under hydrogel scenarios with or without TeEVs exhibited no significant difference in cell viability across all groups (Figure 1I), indicating the good biocompatibility of hydrogels. Moreover, miR-222 was down-regulated in oxygen-glucose deprivation reperfusion (OGDR)-stressed NRCMs, AIRI myocardium, and ischemic reperfusion injury (IRI) post 3 weeks myocardium (Figure S1K). Notably, the expression levels of the miR-222 under the GEL-TeEV treatment were measured to be over 109 times in OGDR-stressed NRCMs (Figure S1L), almost 45 times in AIRI myocardium (Figure S1M) and near 14 times in IRI post 3 weeks myocardium (Figure S1N). Based on adjustable mechanics, controlled release rates, and biocompatible cell survival, the mechanical hydrogels loaded with TeEVs were generated to serve as injectable heart patches in the pericardial cavity.

GEL-TeEVs enhanced cell internalization and rescued apoptosis in OGDR-stressed NRCMs

It has been previously established that CSTSMLKAC cardiac-ischemia-targeting peptide (CTP) can enhance cellular internalization when bonded to EVs.[33] In this study, the targeting uptake ability of TeEVs in NRCMs was evaluated using a fluorescence-labeling assay. The results showed increased red fluorescence in the TeEV group compared to both PBS and miR-222-engineered EV group (Figure 2A), indicating superior uptake ability. The normalized fluorescence intensity corroborated these findings, showing similar results to the fluorescent images (Figure 2B). Further evaluation of targeting internalization was performed using flow cytometry, and the fluorescent curves revealed a marked increase in uptake tendency in the TeEV group (Figure 2C). The quantitatively normalized fluorescence intensity also demonstrated a stronger uptake ability in TeEV cells in OGDR condition (Figure 2D). These internalization results suggested that higher uptake levels of TeEVs could be observed in both control and OGDR-stressed cells, potentially facilitating targeted repair of cardiomyocytes in post-ischemia conditions.

To substantiate the hypothesis regarding the targeting repair ability of TeEV in impaired NRCMs, Tunel staining was employed to monitor apoptosis rescue capabilities in OGDR-stressed NRCMs (Figure 2E). The number of Tunel-positive cells was noticeably reduced following treatment with TeEV and GEL-TeEV, compared to the PBS control in OGDR-stressed conditions. Moreover, the quantitative analysis calculated the proportion of Tunel-positive cells, indicating a decrease in apoptosis levels and revealing efficient OGDR rescue ability for damaged NRCMs (Figure 2F). Furthermore, the expression of apoptosis-related proteins such as Bax, Bcl2, cleaved caspase-3, and caspase-3 was analyzed by western blot (WB) to demonstrate modulation at the protein level (Figure 2G). The WB results indicated that both TeEVs and GEL-TeEVs reduced the Bax/Bcl2 ratio and cleaved caspase-3/caspase-3 ratio in OGDR-stressed NRCMs, illustrating their potent anti-apoptotic effects (Figure 2H). Moreover, the expression levels of the downstream target genes (homeobox containing 1 [Hmbox1], homeodomain interacting protein kinase 1 [HIPK1], and HIPK2) were evaluated. TeEV and GEL-TeEV could decrease the expression levels of Hmbox1 and HIPK2 in OGDR-stressed cells by qPCR analysis (Figure S2A). Furthermore, both Hmbox1 and HIPK2 were also assessed to show the repressive expression levels in TeEV and GEL-TeEV cells by WB analysis (Figure S2B). Nevertheless, HIPK1 was not regulated among these groups (Figure S2C). Thus, these findings support that TeEVs could be specifically targeted and internalized into impaired NRCMs, effectuating high uptake ability and strong anti-apoptosis effects in OGDR-stressed NRCMs.

Myocardial targeting delivery and retention of TeEVs via pericardial hydrogel injection *in vivo*

Given the heart's deep-embedded location within the thoracic cavity, cardiac hydrogel patches represent a promising therapeutic approach for cardiac repair, circumventing the low cardiac targeting and retention associated with intravenous injection.[34–36] Notably, some studies have explored utilizing the pericardium to prevent infection and provide a lubricated chamber for heart protection.[37,38] The pericardial cavity, situated between the serous and fibrous pericardium, is considered an ideal site for hydrogel injection, enabling the construction of hydrogel patches in impaired cardiac tissues.[39,40] Inspired by this conceptualization, we designed an injectable TeEV-loaded pericardial hydrogel patch to enhance myocardial IRI rescue via force-sensing mechanotransduction, delivered in a minimally invasive manner (Figure 3A). After injectable implantation of DiD-labeled miR-222-engineered EV and TeEV with or without hydrogels for 24 h post IRI treatment, mouse hearts were analyzed *ex vivo* using an *in vivo* imaging system spectrum computed tomography imaging system. Fluorescent results indicated that CTP-targeting engineered EVs exhibited stronger fluorescence intensity than non-targeting engineered EVs, regardless of hydrogel usage (Figure 3B). Total radiant efficiency of DiD-labeled fluorescence in CTP-targeting groups (TeEVs and GEL-TeEVs) was measured to be twice as high as that in non-targeting groups (eEVs and GEL-eEVs) (Figure 3C), suggesting that the incorporation of injectable hydrogels did not alter the targeting delivery capability of TeEVs *in vivo*. In addition to cardiac targeting experiment, other organs (liver, spleen, lung, kidney, and brain) were also evaluated to expatiate

CellPress
OPEN ACCESS

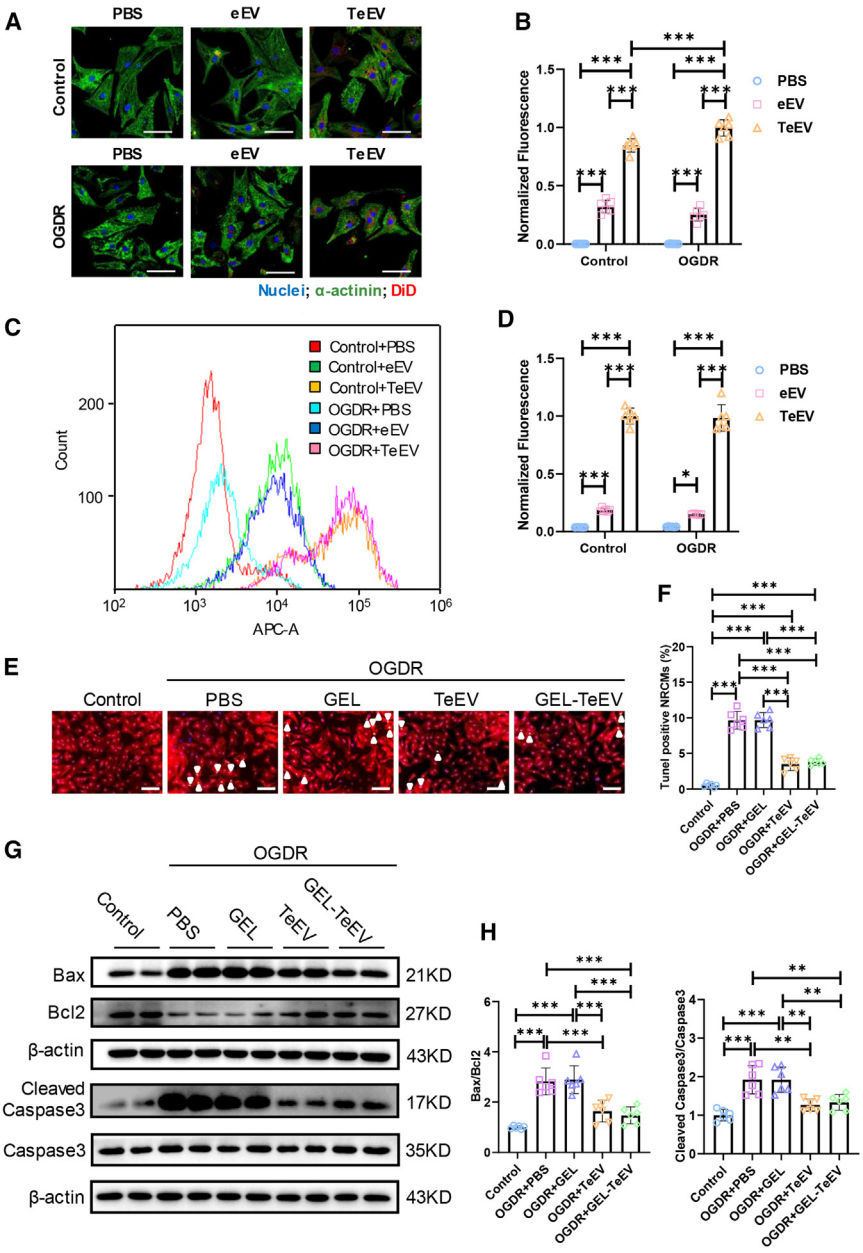

Figure 2. Targeting cell internalization and anti-apoptosis ability of GEL-TeEVs in OGDR-stressed NRCMs

(A) Representative fluorescence images of PBS, miR-222-engineered EV (eEV), and targeting miR-222-engineered EV (TeEV) with or without OGDR-stressed overload. α-actinin: green; DiD: red; nuclei: blue. Scale bar: 50 μm.

(B) Targeting uptake ability calculated by normalized fluorescence intensity.

(C) Flow cytometry evaluation of PBS, eEV, and TeEV with or without OGDR-stressed overload.

(D) Normalized fluorescence quantification by flow cytometry analysis.

(E) Representative fluorescence images of Tunel staining in OGDR-stressed NRCMs. Tunel: green; α-actinin: red; nuclei: blue. The white arrows point to Tunel-positive cells. Scale bar: 100 μm.

(F) Percentage of Tunel-positive cardiomyocytes.

(G) WB estimation for apoptosis-related marker analysis of Bax, Bcl2, cleaved caspase-3, and caspase-3 in OGDR-stressed NRCMs.

(H) Bax/Bcl2 and cleaved caspase-3/caspase-3 ratios from WB analysis in OGDR-stressed NRCMs.

Data present mean ± SD; $n = 6$ per group. Two-way ANOVA test followed by Tukey post hoc test (B, D) and one-way ANOVA test followed by Bonferroni test (F, H) were used for statistical analysis. $^{*}p < 0.05$; $^{**}p < 0.01$; $^{***}p < 0.001$. See also Figure S2.

myocardial targeting ability and metabolic way *in vivo*. It was obvious that strong fluorescence intensity was observed in the liver, independently of other organs (including brain, spleen, kidney, and lung) (Figure S3). To assess the internalization level of targeting engineered EVs in cardiac tissues, we observed that TeEVs accumulated and maintained long-term retention in the base, mid, and apex regions of IRI mouse hearts (Figure 3D). Further evaluation of targeting delivery and retention in cardiac tissues was conducted through cryogenic heart section staining, which revealed increased red DiD-labeled fluorescence in CTP-targeting engineered EVs (TeEVs and GEL-TeEVs) compared to non-targeting engineered EV groups (Figure 3E). Normalized immunofluorescence (IF) efficiency was calculated, and the results demonstrated that the efficiency of CTP-targeting engineered EVs was nearly twice than that of non-targeting engineered EVs (Figure 3F), indicating enhanced cardiac targeting ability, increased internalization efficacy, and deep-tissue retention preference.

The biocompatible hydrogels were injected into the pericardial cavity to solidify a heart-protecting patch *in situ*, and TeEV therapeutics were loaded into hydrogel patches to facilitate slow release for long-term repair of chronic heart diseases. In a mouse IRI model, we conducted an *in vivo* imaging assay of CTP-targeting engineered EVs with or without hydrogels over 3 weeks (Figure 3G). The imaging results suggested that total radiant efficiency decreased in both TeEV and GEL-TeEV groups; however, the release rate of TeEVs was faster than that of GEL-TeEVs, indicating the slow-release functionality of the hydrogel patches (Figure 3H). The normalized area under the curves of total radiant efficiency was assessed, and the area of GEL-TeEVs was calculated to be approximately 3 times higher than that for TeEVs, revealing strong cardiac targeting uptake ability and long-term retention *in situ* after IRI treatment (Figure 3I). Collectively, the injectable TeEV-loaded pericardial hydrogel patch could enhance myocardial targeting delivery and retention of TeEVs and may offer significant therapeutic potential for myocardial IRI rescue.

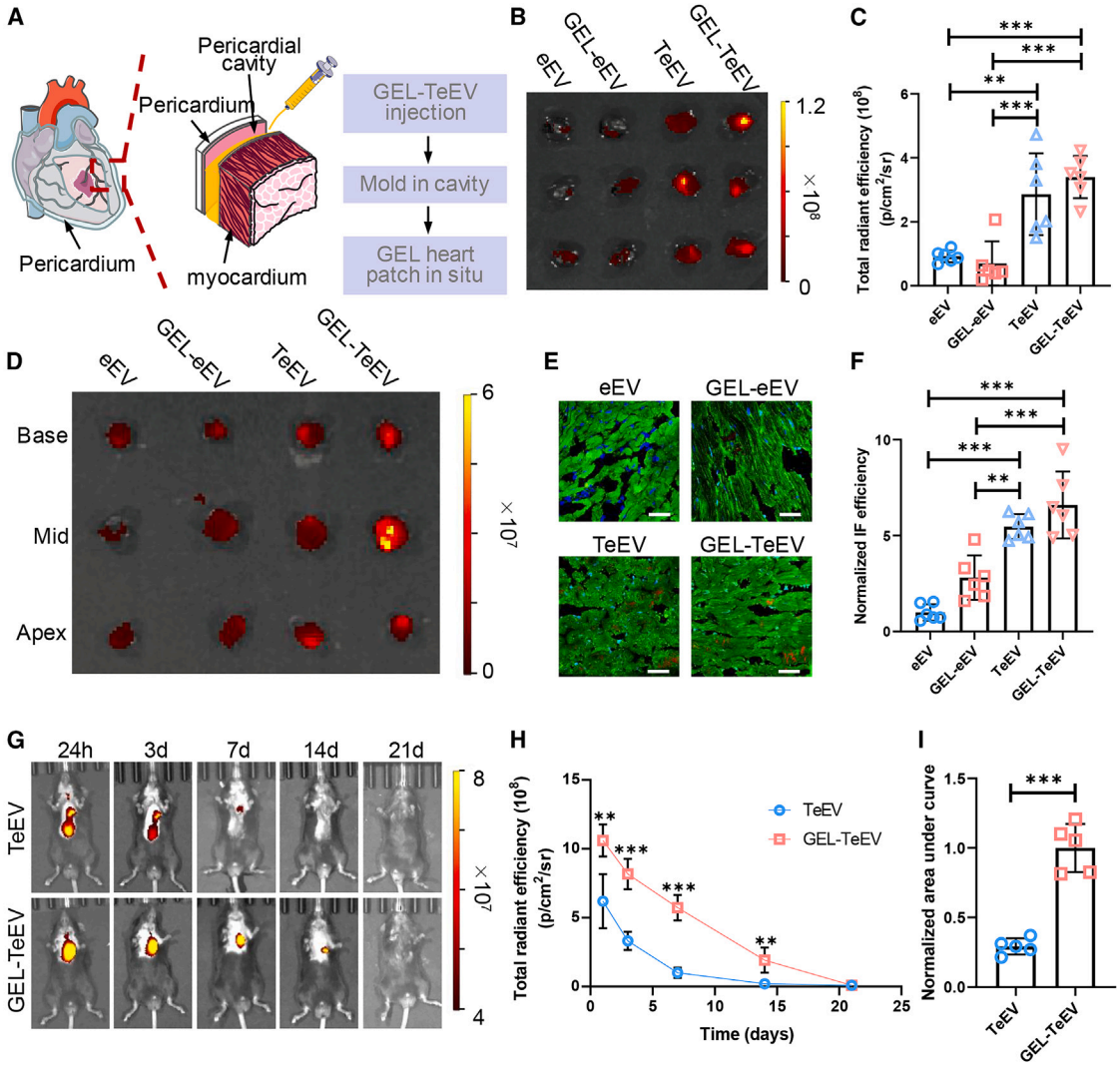

Figure 3. Myocardial targeting delivery and retention of TeEVs via pericardial hydrogel injection *in vivo*

(A) Illustration of minimally invasive injection in pericardial cavity as a natural mold to form cardiac hydrogel patches *in situ*.

(B) Fluorescent images of CTP-targeting engineered EVs (TeEVs) in DiD-labeled hearts.

(C) Total radiant efficiency of DiD-labeled fluorescence in hearts.

(D) Fluorescent images of the cross-sections of IRI hearts from base and mid to apex *in vitro*.

(E) Representative fluorescence images of DiD-labeled eEVs and TeEVs with or without hydrogel patches to detect targeting delivery and retention ability of therapeutics in cardiac tissues. DiD: red; α-actinin: green; nuclei: blue. Scale bar: 50 μm.

(F) Normalized IF efficiency of eEVs and TeEVs to detect internalization efficacy *in vivo*.

(G) Representative *in vivo* fluorescence images of DiD-labeled TeEVs with or without hydrogel patches in mice at 24 h, 3 days, 7 days, 14 days, and 21 days

(H) Total radiant efficiency of quantitative fluorescence intensity in TeEVs and GEL-TeEVs.

(I) Normalized area under the radiant curves of total radiant efficiency.

Data present mean ± SD; $n = 6$ (C–F) or $n = 5$ (H and I) per group. One-way ANOVA test followed by Bonferroni test (C, F) and unpaired Student's t test (H, I) were used for statistical analysis. $^{**}p < 0.01$; $^{***}p < 0.001$. See also Figure S3.

GEL-TeEV patch alleviated acute myocardial IRI

Targeting cardiac ischemia with CTP-ischemia polypeptide-integrated miR-222-engineered EVs represents an efficient therapeutic strategy to attenuate AIRI. These TeEVs were embedded in hydrogels to enhance therapeutic efficiency through mechanical hydrogels. An IRI model was established following 30 min of ischemia, and GEL-TeEV was pericardially injected to form a hydrogel patch within the natural cardiac mold during a 24-h reperfusion period (Figure 4A). To evaluate the therapeutic effectiveness of GEL-TeEV *in vivo*, cardiac 2,3,5-triphenyl tetrazolium chloride (TTC) staining was performed to assess the infarction area post treatment in the IRI model (Figure 4B). The results indicated a significant reduction in the ratio of infarction area to area at risk (INF/AAR) in the GEL-TeEV group, demonstrating

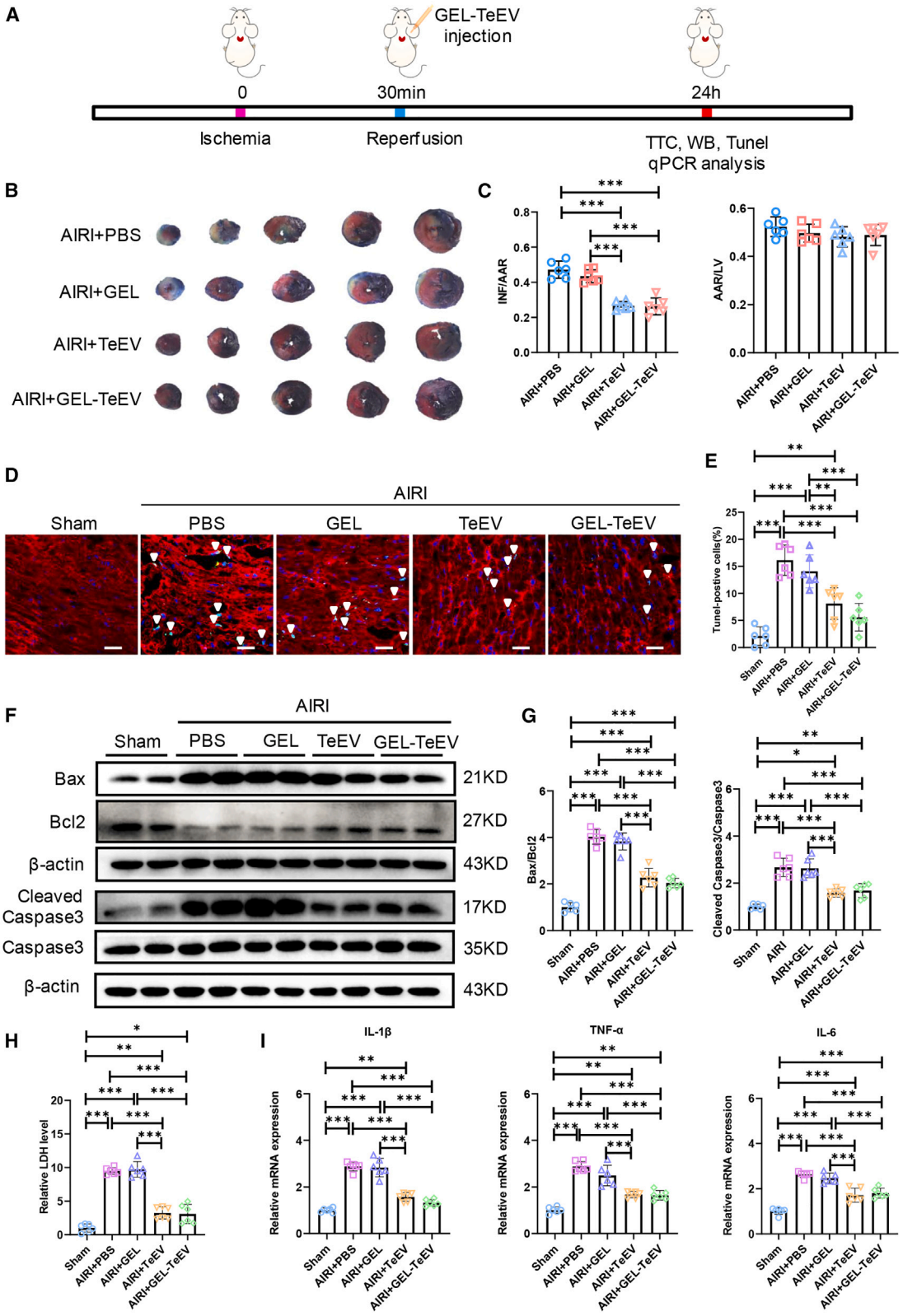

(legend on next page)

decreased infarct size in AIRI (Figure 4C). Notably, a similar INF/AAR ratio was observed between the TeEV and GEL-TeEV groups, suggesting a rapid release of TeEVs from GEL within the first 24 h, which aligns well with the requirements for AIRI treatment. The TTC staining results highlighted a marked decrease in the infarction area due to GEL-TeEV interventional therapy post IRI.

Additionally, apoptosis in cardiomyocytes within myocardial tissues was assessed by Tunel staining, with fluorescent images revealing fewer green Tunel-positive cells evaluated in the GEL-TeEV group compared to the PBS control (Figure 4D). Quantitative analysis of Tunel-positive cells demonstrated a strong apoptosis-inhibiting effect following GEL-TeEV treatment (Figure 4E), with apoptosis similarly reduced in both TeEV and GEL-TeEV groups, indicating sufficient TeEV release from the GEL for AIRI repair. WB analysis was conducted to evaluate the expression levels of apoptosis-related proteins, including Bax, Bcl2, cleaved caspase-3, and caspase-3 (Figure 4F). Consistent with the Tunel results, the ratios of Bax/Bcl2 and cleaved caspase-3/caspase-3 exhibited a decreasing trend in both the TeEV and GEL-TeEV groups (Figure 4G), reflecting significant alleviation of myocardial AIRI. Lactate dehydrogenase (LDH) levels were measured to detect glycolysis-related myocardial injury (Figure 4H), with LDH levels in the GEL-TeEV group dramatically reduced compared to the PBS control, thereby indicating effective AIRI rescue. Moreover, relative expression levels of inflammatory factors such as interleukin (IL)-1β, tumor necrosis factor alpha (TNF-α), and IL-6 were notably elevated in AIRI mice compared to the sham group (Figure 4I). However, TeEV and GEL-TeEV injection effectively down-regulated these pro-inflammatory factors. Besides, the downstream target genes were explored to elucidate that TeEV and GEL-TeEV could down-regulate the expression levels of Hmbox1 and HIPK2 in AIRI mice by qPCR analysis (Figure S4A). Hmbox1 and HIPK2 were further confirmed to be decreased by TeEV and GEL-TeEV treatment by WB analysis (Figure S4B). Meanwhile, HIPK1 was not regulated among these groups (Figure S4C). Hematoxylin & eosin (H&E) immunohistochemical staining confirmed that the structural characteristics of major organs (liver, spleen, lung, and kidney) remained unchanged, suggesting minimal systemic toxicity from biocompatible GEL incorporation (Figure S4D). In conclusion, the GEL-TeEV patch formed by *in situ* pericardial injection could precisely target the ischemic region to alleviate AIRI.

GEL-TeEV patch ameliorated cardiac dysfunction in cardiac IRI remodeling

The targeting-engineered EVs were encapsulated in GEL to facilitate slow release for chronic IRI rescue via a minimally invasive injection method. To validate the hypothesis that GEL-TeEV patch mitigates cardiac IRI dysfunction, an IRI model was induced with 30 min of ischemia followed by 3 weeks of reperfusion, treated with GEL-TeEV injection (Figure 5A). Echocardiography was performed to assess heart function (Figure 5B). Left ventricular ejection fraction (Figure 5C) and fractional shortening (Figure 5D) in the GEL-TeEV group showed significant improvements compared to the IRI control, ameliorating cardiac IRI remodeling. Masson's trichrome staining was utilized to evaluate the level of cardiac fibrosis after the treatment with GEL-TeEV therapeutics (Figure 5E). The fibrosis area (18.61% ± 2.83%) in the IRI model was reduced to 6.77% ± 1.40% in the GEL-TeEV-treated group (Figure 5F). Furthermore, the expression of fibrosis-related protein alpha-smooth muscle actin (α-SMA) was explored by WB analysis (Figure 5G). There was an elevated expression of α-SMA in the IRI model, whereas these proteins showed a decreasing trend in the GEL-TeEV group. Quantitative results confirmed that α-SMA was up-regulated following IRI induction (Figure 5H), and their expression was mitigated by GEL-TeEV treatment, delaying fibrosis-related protein expression to improve cardiac dysfunction. The expressions of two additional fibrosis-related genes, collagen type I alpha 1 chain (Col1a1, Figure 5I) and collagen type III alpha 1 chain (Col3a1, Figure 5J), were also quantified using qPCR analysis, showing reduced expression in the GEL-TeEV group, consistent with the WB results for α-SMA. Pathological cardiac genes such as atrial natriuretic peptide (ANP), brain natriuretic peptide (BNP), and beta-myosin heavy chain (β-MHC) were significantly increased in the IRI model, but their expression was suppressed by GEL-TeEV therapeutics, demonstrating the amelioration of cardiac IRI remodeling (Figure 5K). Meanwhile, the downstream target genes of miR-222 were also proved to reveal the long-term depressant expressions of Hmbox1 and HIPK2 in cardiac IRI remodeling under GEL-TeEV treatment by qPCR analysis (Figure S5A). WB analysis of Hmbox1 and HIPK2 displayed that the expression levels of both key downstream genes were persistently repressed under GEL-TeEV treatment (Figure S5B). Nevertheless, HIPK1 was not affected among these groups (Figure S5C). Additionally, H&E staining revealed that the evolution of pathologically enlarged myocardial cells induced by IRI remodeling was mitigated in the GEL-TeEV-treated mice, preventing the

Figure 4. GEL-TeEV patches alleviated myocardial acute IRI

(A) Establishment of AIRI model after 30-min ischemia and then protected by GEL-TeEV patches followed by 24-h reperfusion *in vivo*.

(B) Cardiac 2,3,5-triphenyl tetrazolium chloride (TTC) staining.

(C) Detection of the infarction area/area at risk (INF/AAR) ratio and the area at risk/left ventricle weight (AAR/LV) ratio after AIRI.

(D) Representative fluorescence images of Tunel staining in myocardial tissues. Tunel: green; α-actinin: red; nuclei: blue. The white arrows point to Tunel-positive cells. Scale bar: 100 μm.

(E) Percentage of Tunel-positive cells.

(F) WB estimation for apoptosis-related marker analysis of Bax, Bcl2, cleaved caspase-3, and caspase-3.

(G) Bax/Bcl2 and cleaved caspase-3/caspase-3 ratios from WB analysis.

(H) Lactate dehydrogenase (LDH) expression level.

(I) Relative expression levels of inflammatory factors, including IL-1β, TNF-α, and IL-6.

Data present mean ± SD; $n = 6$ per group. One-way ANOVA test followed by Bonferroni test was used for statistical analysis. $^{*}p < 0.05$; $^{**}p < 0.01$; $^{***}p < 0.001$. See also Figure S4.

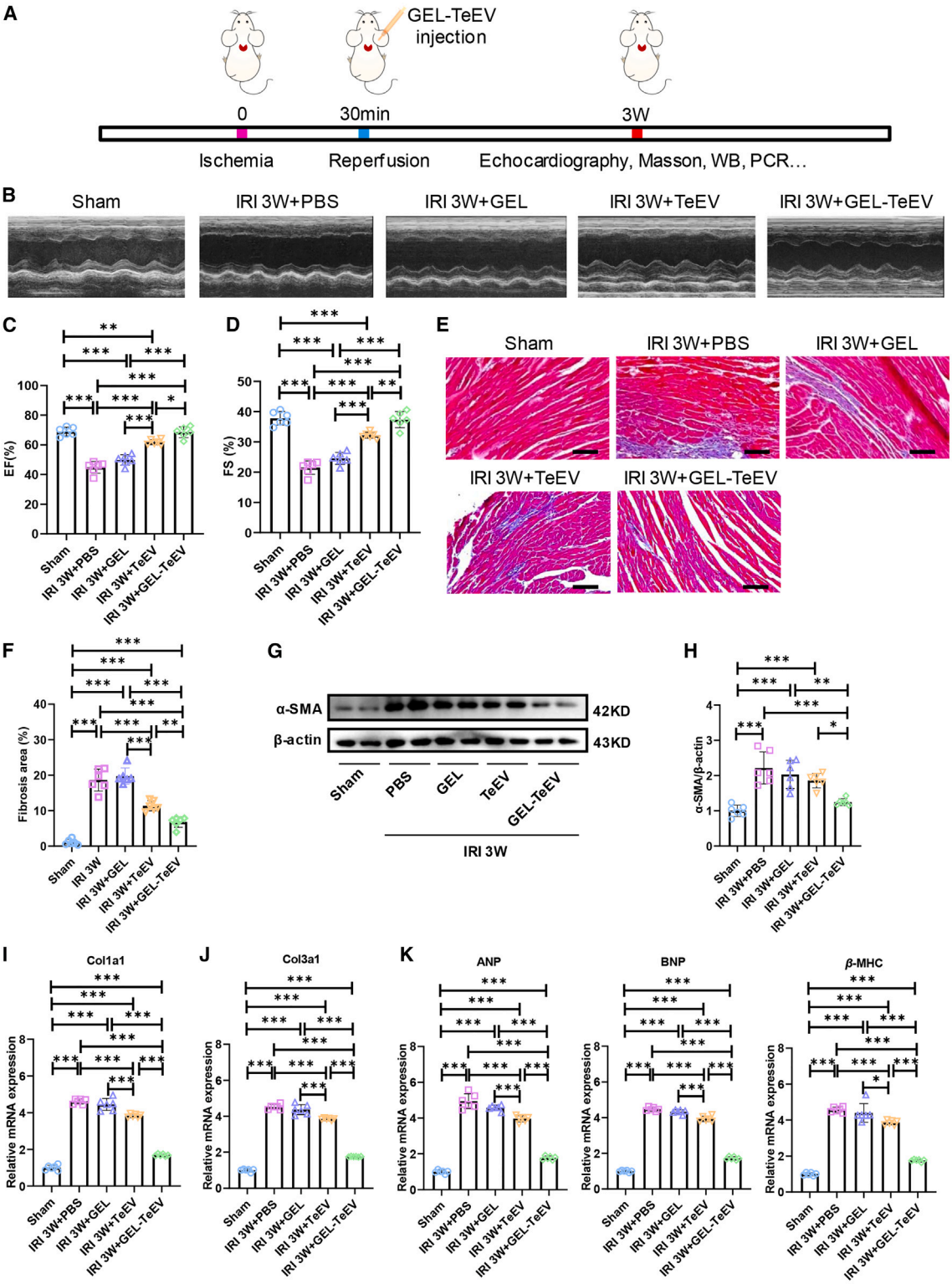

Figure 5. GEL-TeEV patches ameliorated cardiac dysfunction in cardiac IRI remodeling

(A) Establishment of IRI remodeling model after 30-min ischemia and then protected by GEL-TeEV patches followed by 3-week reperfusion *in vivo*.

(B) Representative echocardiography images of sham, IRI+PBS, IRI+GEL, IRI+TeEV, and IRI+GEL-TeEV groups.

(C) Left ventricle ejection fraction (EF).

(legend continued on next page)

progression of cardiac hypertrophy (Figure S5D). Collectively, these results demonstrate that GEL-TeEV patches, implanted via *in situ* minimally invasive injection, could inhibit the progression of cardiac fibrosis and protect against cardiac pathological remodeling.

GEL-TeEV patches activated intracellular mechanotransduction in the heart

Force-sensing biophysical stimuli play a vital role in regulating cardiac morphogenesis and cytoskeletal distribution of myocardial cells.[41] Beyond immediate cell-cell interactions, myocardial cells are capable of discerning various extracellular mechanical cues such as stretching mechanics, fluidic hemodynamics, and ECM substrate rigidity, which enable them to respond adaptively to environmental changes.[42] When mechanical forces overload myocardial cells, integrin-adhesion-coupling receptors (IACRs) are activated, influencing cellular features and behaviors, such as morphology, division, migration, and internalization.[43–45] Integrin expression was analyzed to assess IACR formation in a 3-week IRI mouse model (Figure 6A). Quantitative fluorescence intensity, in both total integrin and per-cell measurements (Figure S6A), indicated enhanced IACR accumulation on lipid raft microdomains. IACRs were observed interacting with focal adhesions (FAs) under force-driven mechanical stimuli from GEL patches. Vinculin, a primary component of FA, was assessed via WB analysis to evaluate its assembly in GEL-TeEV-treated mice (Figure 6B). The results revealed that vinculin expression declined during IRI remodeling, while GEL-TeEV patches restored vinculin assembly (Figure 6C), promoting intracellular cytoskeletal organization in cardiomyocytes. Talin-1, another FA structural protein, anchors connections in the plasma membrane to interact with IACRs and sense extracellular mechanical tension induced by GEL-TeEV patches. Fluorescent imaging of talin-1 (Figure 6D) showed the increasing intensity following GEL-TeEV treatment, with the lowest intensity observed in the IRI control (Figure S6B). Magnification images revealed increased aggregation of talin-1 proteins in the hearts of GEL-TeEV mice (Figure S6C), suggesting that GEL-TeEV patches could enhance the expression of adhesion coupling receptors such as integrin, vinculin, and talin-1, thereby promoting intracellular cytoskeleton formation.

Myosin, a motor cytoskeletal protein linked to actin or actinin, is activated by adhesion proteins. It provides driving force from GEL patches for efficient TeEV internalization in myocardial cells. Fluorescent imaging of myosin demonstrated increased myosin intensity in GEL-TeEV mice (Figures 6E and S6D). The heterogeneous distribution of adhesion proteins and the cytoskeleton led cells to open mechanical cationic channels (Piezo1), causing calcium influx due to the overloaded tension in IRI remodeling. Enhanced Piezo1 expression was noted in IRI remodeling under hemodynamic stress, while the force-protecting GEL patch and TeEV release therapeutics alleviated the IRI-overloaded mechanics (Figures 6F and S6E). Moreover, the Young's modulus of cardiac tissues was measured to analyze heart stiffness in different groups (Figure 6G). Conversely, adhesion force in cardiac tissues was enhanced by GEL-TeEV treatment, ameliorating adhesion function of the myocardium (Figure 6H). The results indicated a significant increase in Young's modulus in IRI hearts due to elevated fibrosis levels, whereas stiffness in GEL-TeEV cardiac tissues decreased, reflecting mechanical and synergistic protection. These mechanical results suggest that myocardial cells could undergo stress overload homeostasis during IRI, while GEL-TeEVs acted as mechanical preservers and therapeutics, rescuing abnormal motor myosin assembly, pressure-sensitive Piezo1 expression, fibrosis-related rigid expansion, and adhesion force decline in the IRI model.

Yes-associated protein (YAP) has been studied for its role in transmitting biomechanical changes from the cytoplasm to the nucleus via the Hippo signaling pathway.[46,47] YAP expression was analyzed to regulate intracellular mechanotransduction in myocardial cells (Figure 6I). In IRI mice, YAP expression was suppressed due to damaged cytoskeletal structures, which impeded excitation-contraction (E-C) coupling in cells (Figure 6J). GEL-TeEV patches, serving as mechanical and gene protectors, rehabilitated E-C coupling formation and enhanced YAP-related mechanotransduction. This mechanical contractility was further transmitted into the nucleus, affecting nuclear skeleton distribution. LaminA/C was evaluated by WB to analyze nuclear import and recruitment influenced by cytoskeletal stiffening and YAP-induced mechanotransduction (Figure 6K). The quantitative results showed increased laminA and laminC expression levels in GEL-TeEV mice, providing resistance to nuclear deformation and enhancing chromatin activity (Figure 6L). These results indicate that GEL-TeEVs could enhance force-sensing mechanotransduction through YAP modulation, improving nuclear laminA/C structural integrity for effective IRI repair.

Furthermore, TeEV and patches could also arouse mechanical protein expression in AIRI mice. WB analysis showed that vinculin expression was decreased in AIRI mice (Figure S6F). After the treatment of GEL-TeEV patches, the expression level of vinculin was enhanced to induce intracellular cytoskeletal assembly in cardiomyocytes. Talin-1 was stained to reveal the interaction of FAs and IACRs in AIRI model. Fluorescent imaging of talin-1 (Figure S6G) presented the enhanced fluorescence intensity under GEL-TeEV treatment, while the lowest intensity was observed in the AIRI group (Figure S6H). These FA proteins could affect

(D) Fractional shortening (FS).
(E) Masson staining. Scale bar: 100 μm.
(F) Cardiac fibrosis detected by Masson staining.
(G) WB analysis of fibrosis-related protein (α-SMA).
(H) Quantitative protein expression level of α-SMA.
(I) Col1a1 gene expression level quantified by qPCR analysis.
(J) Col3a1 gene expression level quantified by qPCR analysis.
(K) Relative expression level of pathological cardiac genes, including ANP, BNP, and β-MHC.
Data present mean ± SD; $n = 6$ per group. One-way ANOVA test followed by Bonferroni test was used for statistical analysis. $^{*}p < 0.05$; $^{**}p < 0.01$; $^{***}p < 0.001$. See also Figure S5.

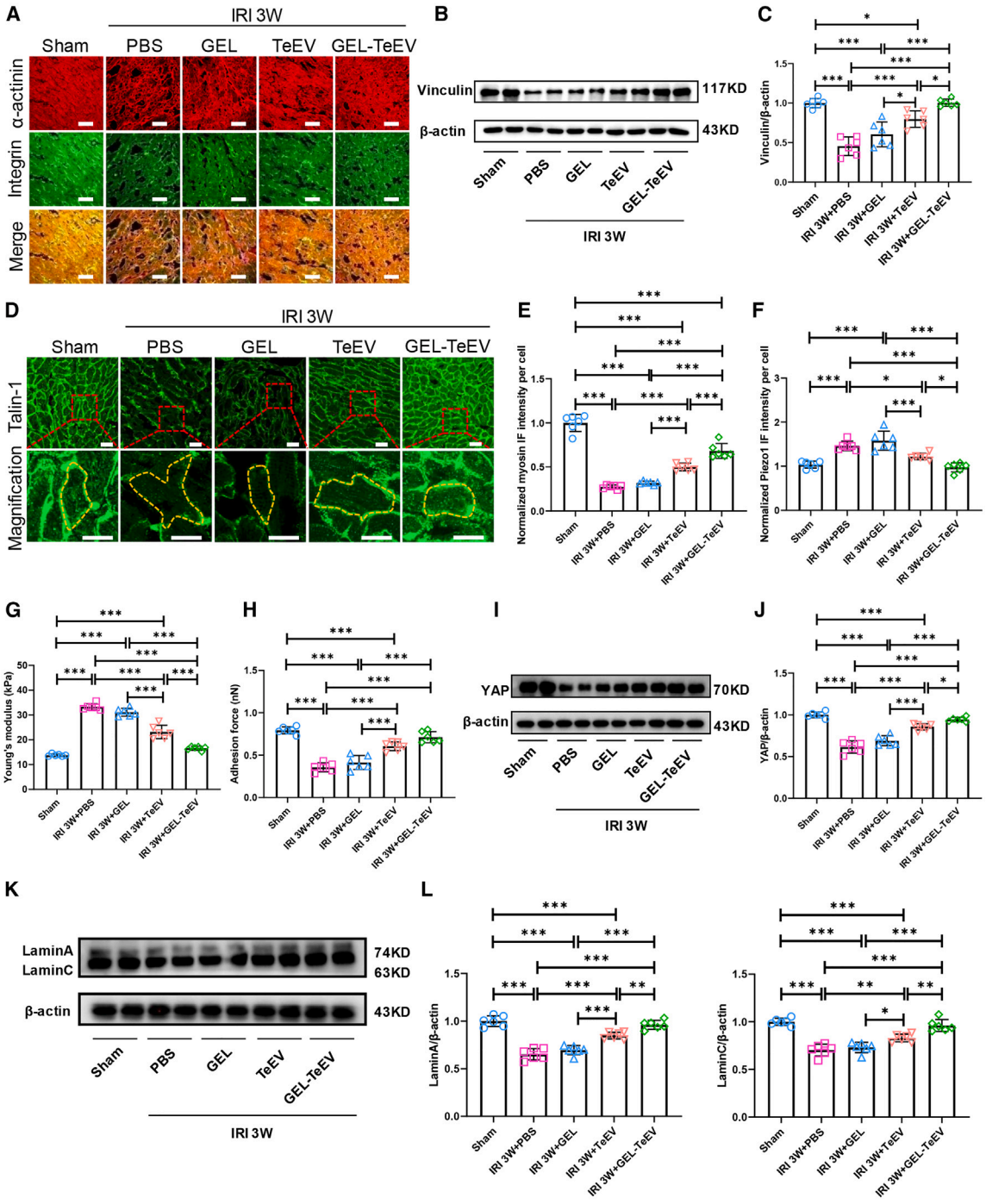

Figure 6. Activation of GEL-TeEV patches on intracellular adhesion-cytoskeleton-nucleus mechanotransduction of myocardial cells *in vivo*

(A) Representative fluorescence images of integrin (green). α-actinin: red; nuclei: blue. Scale bar: 100 μm.

(B) WB analysis of vinculin to detect focal adhesion formation.

(C) Quantitative vinculin expression level by WB analysis.

(D) Representative fluorescence images of talin-1 (green). Scale bar: 100 μm. Magnified talin-1 images were shown in the second row. Scale bar: 50 μm.

(E) Normalized myosin immunofluorescence (IF) intensity per cell.

(F) Normalized Piezo1 IF intensity per cell.

(G) Young's modulus of cardiac tissues measured by AFM.

(H) Adhesion force of cardiac tissues.

(I) WB analysis of YAP.

(legend continued on next page)

intracellular cytoskeletal distribution and motor protein formation. Fluorescent imaging of myosin (Figure S6I) showed the increased fluorescence intensity under GEL-TeEV treatment (Figure S6J). The overload stress of AIRI induced mechanical cationic Piezo1 channel to cause calcium influx. Fluorescent imaging of Piezo1 (Figure S6K) indicated that increasing Piezo1 expression was observed in AIRI mice. After the patch and TeEV treatment, AIRI-induced stress overload was relieved by reducing Piezo1 expression (Figure S6L). YAP-related Hippo pathway was also evaluated to explain the enhanced YAP mechanotransduction by WB analysis (Figure S6M). Nuclear skeleton structures were further controlled by mechanical E-C coupling stimulation. LaminA/C was explored to present the increasing expression levels after the treatment of GEL patches and TeEV therapeutics (Figure S6N). Thus, the data present that GEL patches and TeEV therapeutics could promote YAP mechanotransduction and increase nuclear laminA/C expression by FA formation and cytoskeleton distribution to ameliorate cardiac function.

Underlying mechanism of GEL-TeEV patches for enhanced nanomechanics in NRCMs

To elucidate the underlying mechanisms behind the observed IRI rescue via cytoskeleton remodeling and nuclear mechanotransduction, we investigated the coordinated actions of mechanical signaling activation pathways in NRCMs. Cells were cultured under conditions of medium alone, GEL, TeEV, and GEL-TeEV to evaluate FA formation by vinculin staining (Figure 7A). Fluorescent imaging demonstrated enhanced FA formation in cells treated with GEL-TeEV. Both normalized total vinculin IF intensity (Figure S7A) and average IF intensity per cell (Figure 7B) were elevated under GEL-TeEV therapy, indicative of GEL protection and targeted TeEV repair. Cytoskeleton structures were well organized, as shown by motor protein myosin staining (Figure S7B). The normalized myosin IF intensity displayed an increased trend under GEL-TeEV treatment (Figures 7C and S7C), mirroring the results observed with FA assembly. Stiffening of cell culture plates (CCPs) was found to provoke an inflammatory response, promoting pressure-stress overload in NRCMs. Mechanical cationic channel Piezo1 was overexpressed in CCP control, while its excess was restrained by GEL-TeEV incorporation (Figures 7D, S7D, and S7E). Differences in FA, cytoskeleton, and force-sensing channels could contribute to intracellular nanomechanics. AFM was utilized to measure force-distance curves, evaluating the nanomechanics of NRCMs (Figure S7F). Cells progressively stiffened under GEL-TeEV treatment due to well-organized cytoskeletal structures, contrasted by a reduction in stiffness without GEL or TeEVs (Figure 7E). The adhesion force against silicon nitride nanoparticles on the AFM probe was reduced with GEL-TeEV incorporation (Figure 7F). Further, YAP results also revealed nuclear translocation by nucleus/cytoplasm ratio in the control group, while YAP signals were enriched in the cytoplasm by GEL-TeEV treatment (Figure 7G). The quantitative analysis of nuclear YAP showed a decreasing trend in the GEL-TeEV group (Figure 7H). These results demonstrated that GEL-TeEV patches could modulate cellular nanomechanics through cytoskeletal repair and YAP nuclear-cytoplasmic translocation, activating force-related signaling pathways to enhance the uptake of TeEV therapeutics (Figure 7I). The mechanism by which GEL-TeEV patches rescue IRI involves GEL hydrogels enhancing cardiac ECM functions to activate E-C coupling, establishes contractile myosin, and promotes ultrastructural remodeling. This improves metabolic or mitochondrial function, facilitating the effective internalization of TeEVs. Collectively, TeEVs are released slowly from mechanical hydrogels and internalized into myocardial cells, improving IRI and cardiac remodeling through the regulation of mechanical signal activation, adhesion protein assembly, cytoskeleton-mediated formation, force-sensing channel opening, and nuclear mechanotransduction.

DISCUSSION

Cardiovascular tissue engineering offers a promising approach to mitigating myocardial injury by promoting cardiac repair.[48–53] Hydrogel patches have emerged as effective tools in this strategy. They can protect against disease-induced stress overload by influencing mechanotransduction pathways, shielding the heart from excessive mechanical stress, and serving as carriers for drugs that counteract cardiac pathological remodeling.[54] Current implantation of cardiac patches necessitates open-chest surgery, a highly invasive procedure. Recently, minimally invasive injection techniques have been proposed for delivering cardiac patches *in situ*.[40,55–57] However, this method often relies on shape-memory biomaterials, which may disrupt the pericardium, a crucial structure for maintaining heart stability after injury. *In situ* injectable hydrogel patches offer a solution. This approach holds significant promise for achieving minimal invasiveness in cardiac regeneration and repair.[58,59] Viscoelastic heart patches made from adhesive epicardial hydrogels can improve outcomes in MI by enhancing the mechanical integrity of left ventricular tissues.[60,61] Acellular epicardial patches formed through ionic crosslinking have demonstrated efficacy in reversing both acute and subacute MI due to their low dynamic modulus, which optimizes the balance between the fluid and solid properties (gel point) of hydrogels during left ventricular remodeling.[10]

Cardiac IRI exacerbates pathological hypertrophy and cardiac fibrosis, ultimately leading to HF.[62] Cardiomyocytes initially respond to biomechanical stimuli (physiological or pathological), by expanding their surface area (hypertrophy). However, prolonged excessive tension can lead to irreversible heart decompensation and various cardiac dysfunctions.[63–66] Mechanotransduction, the process by which mechanical forces are converted into cellular signals, is considered a critical factor in heart diseases triggered by mechanical stresses like shear

(J) Quantitative YAP expression level.
(K) WB analysis of laminA/C to detect nuclear skeleton structures.
(L) Quantitative laminA/C expression level.
Data present mean ± SD; $n = 6$ per group. One-way ANOVA test followed by Bonferroni test was used for statistical analysis. $^{*}p < 0.05$; $^{**}p < 0.01$; $^{***}p < 0.001$. See also Figure S6.

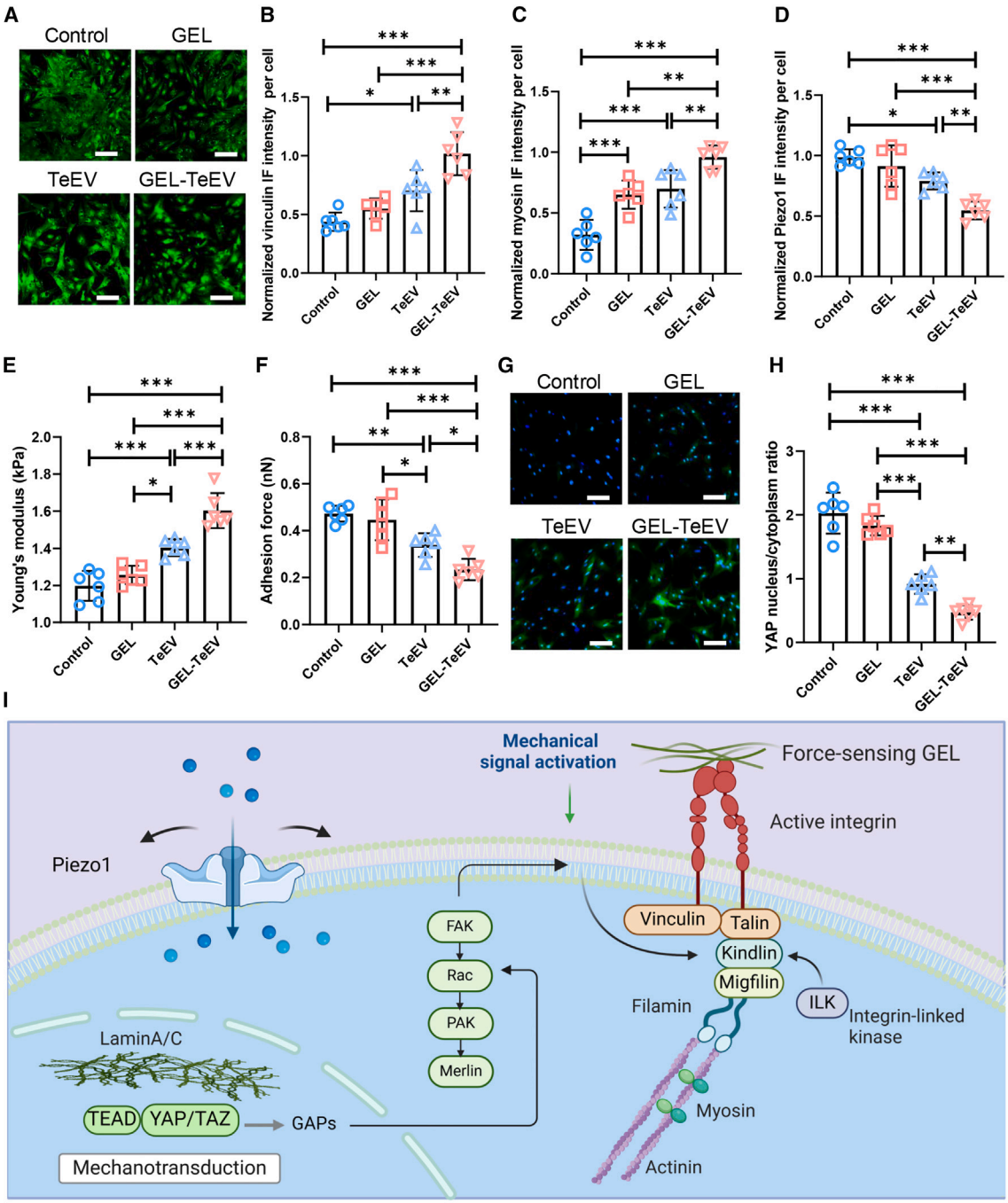

Figure 7. Enhanced nanomechanics by GEL-TeEV patches in NRCMs to induce cell focal adhesion formation and well-organized cytoskeleton structures for force-activated uptake of TeEVs

(A) Representative fluorescence images of vinculin (green). Scale bar: 100 μm.
(B) Normalized vinculin IF intensity per cell.
(C) Normalized myosin IF intensity per cell.
(D) Normalized Piezo1 IF intensity per cell.
(E) Young's modulus of NRCMs measured by AFM.
(F) Adhesion force of NRCMs.
(G) Representative fluorescence images of YAP (green). Nuclei: blue. Scale bar: 100 μm.
(H) YAP nucleus/cytoplasm ratio of NRCMs.

(legend continued on next page)

stress, stretching tension, and hemodynamic overload.[67] To protect cardiac mechanotransduction against IRI, injectable GEL hydrogels were developed. These hydrogels are injected into the pericardial cavity to reinforce IRI-induced cardiac repair. An alternative approach utilizes miR-222-engineered EVs designed using the ischemic CSTSMLKAC polypeptide. These EVs function as gene-mediated therapeutic nanoparticles and are loaded into mechanical hydrogels to alleviate heart dysfunction after IRI. Compared to stem cell therapy, EVs or exosomes derived from stem cell-free sources offer advantages by avoiding ethical concerns and immune rejection issues while still improving outcomes in IRI. These targeted EVs have been shown to enhance post-IRI repair by delivering therapeutic components to mitochondria.[68] The combination of CSTSMLKAC polypeptide (PEP) and triphenylphosphonium cations (TPP+) effectively binds to the mitochondria, forming a PEP-TPP-mitochondria complex that facilitates efficient uptake by cardiomyocytes during IRI repair. These complexes promote cardiac function by enhancing energy production, strengthening mechanical contraction, reducing cell apoptosis, and mitigating inflammatory responses.

Force-sensing mechanotransduction may be considered as an underlying mechanism for IRI repair in the cardiovascular system.[69] Cardiomyocytes are embedded within the ECM of myocardial tissue, where they sense mechanical cues that direct ECM remodeling, adhesion-dependent receptor activation, cytoskeletal reorganization, and nuclear mechanotransduction.[70] Firstly, integrins serve as initial anchors, tethering cells to the ECM and forming clustered FAs, which function as multiprotein signaling hubs.[71–73] FA kinase and steroid receptor coactivator (SRC) are key downstream effectors that orchestrate various cellular functions.[74] FAs mediate morphological changes in cells through actin polymerization-driven expansion and myosin-dependent contraction, thereby enhancing the internalization of EVs by cardiomyocytes.[75] These evidences show that the cardiac GEL-TeEV patches could alleviate early IRI and activate adhesion-cytoskeleton-related mechanical signals to further promote TeEV uptake in IRI hearts. More TeEVs were internalized into cardiac cells to release protective miR-222 for IRI rescue. As the positive feedback, due to the successful protection of TeEVs to the damaged hearts, force-related signals were further stimulated to produce more FA, reorganize cytoskeleton structures, and activate nuclear mechanotransduction for improving the functions of myocardial cells. Polymerization of F-actin filaments (F-actin) reduces the availability of G-actin, leading to decreased association with myocardin-related transcription factor A (MRTFA). Consequently, MRTFA translocates to the nucleus, where it interacts with serum response factor to regulate gene transcription, critical for metabolic reprogramming, proliferation, and cellular responses to mechanical stimuli.[76] Secondly, in addition to integrin signaling, transient receptor potential vanilloid type 4 and Piezo1 cation channels are stimulated by mechanical forces exerted on the plasma membrane.[77] Their changes affect calcium (Ca^{2+}) influx, which influences numerous transcription factors, mechanical signaling pathways, and cytoskeletal reorganization, ultimately contributing to force-sensing protection against heart diseases. Thirdly, mechanical force induces the inhibition of the classical Hippo pathway, leading to nucleus-cytoplasm translocation of YAP to promote gene expression for enhanced cellular functions.[78] These genes are involved in cellular metabolic reprogramming, proliferation, and responsiveness to mechanical stimuli through interaction with the transcriptional enhanced associate (TEA) domain transcription factor family in cardiac tissues. Mechanotransduction is also directly propagated from the cytoskeleton to the nuclear envelope via laminA/C and linker of nucleoskeleton and cytoskeleton (LINC), comprising transmembrane proteins SUN and nesprin.[79] The LINC complexes play a role in mediating nuclear morphology, chromatin organization, gene regulation, and nuclear pore permeability. This function facilitates the nucleus-cytoplasm translocation of YAP and MRTFA during IRI remodeling. Therefore, force-sensing mechanics and tension are considered as the crucial factors for cardiovascular regeneration and repair.

Under the protection of GEL-TeEV hydrogel patches, the porous GEL structures facilitated the rapid release of more than half of the TeEVs from the hydrogel network within the first 3 days. The released TeEVs were delivered into myocardial cells, promoting their uptake through the activation of a cytoskeleton-induced cationic signaling pathway triggered by mechanical stimuli. Engineered EVs have been shown to have therapeutic effects, including alleviating myocardial IRI.[80,81] The overexpression of RNAs (mRNA, lncRNA, and miRNA) and functional proteins within these EVs can modulate cell-to-cell communication and stimulate cell migration, thereby promoting angiogenesis in cardiac tissue.[82] In this study, TeEVs were employed to reduce cardiac apoptosis. In this process, GEL-TeEV patches could promote cytoskeleton formation of cardiomyocytes to increase cell stiffness (Young's modulus), and the increased nanomechanics could provide driving force for TeEV internalization. More TeEVs alleviated cardiac fibrosis in IRI remodeling post 3 weeks, thus reducing cardiac mechanics. These effects were achieved through minimally invasive surgical delivery using a mechanical hydrogel. Overall, the study demonstrates that targeted, engineered TeEVs released from mechanical hydrogel patches could be delivered into myocardial cells to improve AIRI and cardiac remodeling by regulating mechanical signaling activation, adhesion-related protein assembly, cytoskeleton force channel opening, and nuclear mechanotransduction.

In brief, injectable pericardial hydrogel patches loaded with TeEVs were constructed to alleviate myocardial IRI. Grafting of the methacryloyl group into gelatin was successfully confirmed by chemical analysis and gelatinization. HUC-MSC-derived EVs were engineered to overexpress miR-222. These TeEV therapeutics were achieved through ischemic CTP modification. TeEVs demonstrated high uptake in NRCMs and myocardial

(I) Mechanical hydrogel patches were used to induce FA-coupling receptor formation, cytoskeletal nanomechanics, and nuclear mechanotransduction for mechanical signaling activation and to promote TeEV uptake for IRI repair.

Data present mean ± SD; $n = 6$ per group. One-way ANOVA test followed by Bonferroni test was used for statistical analysis. $^{*}p < 0.05$; $^{**}p < 0.01$; $^{***}p < 0.001$. See also Figure S7.

tissues *in vivo*. The GEL-TeEV cardiac patches were injected into the pericardial cavity using a minimally invasive approach to rescue IRI. The rapid release of TeEVs from the hydrogels within the first 24 h enhanced the rescue of AIRI. Furthermore, the slow release of controlled TeEVs at 3 weeks alleviated heart dysfunction post IRI remodeling. TeEVs reduced myocardial apoptosis, cardiac fibrosis, and the immune inflammatory response. Targeted and engineered TeEVs were controllably released from the mechanical hydrogel patches and delivered precisely into cardiomyocytes to ameliorate ischemic myocardial diseases. This was achieved by regulating mechanical signaling activation, adhesion-related protein assembly, cytoskeleton force channel opening, and nuclear mechanotransduction. This study has the potential to expand our understanding of therapeutic-loaded cardiac patches and force-sensing mechanotransduction in heart tissue repair.

Limitations of the study

GEL-TeEV cardiac patches have some limitations. These patches were examined to evaluate the rescue ability of damaged cells *in vitro* and to reveal the therapeutic effect of cardiac patches in the male C57BL/6 mouse model *in vivo*. Nevertheless, the non-human primates were not performed in this study, due to resource, technology, and time restrictions. Long-term TeEV retention effect (over three weeks) is not executed due to the degradability of mechanical hydrogel model. Moreover, the potential off-targeting effects of TeEVs may partially occur in non-cardiac cells, such as fibroblasts and endothelial cells.

RESOURCE AVAILABILITY

Lead contact

Further information and requests for resources and reagents should be directed to and will be fulfilled by the lead contact, Prof. Junjie Xiao (junjiexiao@shu.edu.cn).

Materials availability

All reagents generated in this study are accessible from the lead contact with a completed Materials Transfer Agreement.

Data and code availability

- All data reported in this paper will be shared by the lead contact upon reasonable request.
- This paper does not report original code except ^{1}H-NMR. The raw data of ^{1}H-NMR are deposited on Protein DataBank under the accession number Gelatin BMRB ID: 26354 and GelMA BMRB ID: 26355.
- Any additional information required to reanalyze the data reported in this work paper is available from the lead contact upon reasonable request.

ACKNOWLEDGMENTS

This work was supported by grants from the National Key Research and Development Project (2022YFA1104500 to J.X.), National Natural Science Foundation of China (82020108002 and 82225005 to J.X., 82302401 to Y.W., and 82200321 to Q.Z.), Science and Technology Commission of Shanghai Municipality (23410750100 to J.X.), the "Dawn" Program of Shanghai Education Commission (19SG34 to J.X.), and Shanghai Sailing Program (21YF1413200 to Q.Z.).

AUTHOR CONTRIBUTIONS

Conceptualization, Y.W., Q.Z., and J.X.; methodology, Y.W., D.M., X.S., and Y.H.; validation, Y.W., Q.Z., and J.X.; visualization, Y.W., D.M., X.S., and Y.H.; writing – original draft, Y.W. and J.X.; writing – review and editing, all authors; funding acquisition, Y.W., Q.Z., and J.X.; resources, Y.W., Q.Z., and J.X.; supervision, J.X.

DECLARATION OF INTERESTS

The authors declare no competing interests.

STAR★METHODS

Detailed methods are provided in the online version of this paper and include the following:

- KEY RESOURCES TABLE
- EXPERIMENTAL MODEL AND STUDY PARTICIPANT DETAILS
- METHOD DETAILS
  - Chemical synthesis of viscoelastic GEL precursors
  - ^{1}H nuclear magnetic resonance (^{1}H-NMR) analysis
  - Cell culture and targeting miR-222-engineered EV construction
  - Transmission electron microscope (TEM)
  - GEL-based hydrogel fabrication
  - Observation of hydrogel morphology
  - Mechanical measurement of stiffness and adhesive force
  - Equilibrium absorption ratio
  - Weight loss of hydrogel by enzymatic degradation
  - TeEV release profile in GEL
  - Cellular internalization of TeEVs in neonatal rat cardiomyocytes
  - Cell viability assay
  - Tunel staining and apoptosis analysis of NRCMs
  - Intrapericardial injection
  - 2,3,5-Triphenyl tetrazolium chloride (TTC) staining
  - Myocardial apoptosis evaluation
  - Lactate dehydrogenase (LDH) assay
  - Hematoxylin & eosin (H&E) and masson's trichrome staining
  - Heart function analysis
  - Real-time quantitative PCR (RT-qPCR)
  - Mechanical signaling analysis of adhesion proteins, cytoskeleton and YAP
- QUANTIFICATION AND STATISTICAL ANALYSIS

SUPPLEMENTAL INFORMATION

Supplemental information can be found online at https://doi.org/10.1016/j.xcrm.2025.101987.

Received: October 10, 2024
Revised: December 5, 2024
Accepted: February 3, 2025
Published: March 3, 2025

REFERENCES

1. Toldo, S., and Abbate, A. (2024). The Role of the Nlrp3 Inflammasome and Pyroptosis in Cardiovascular Diseases. Nat. Rev. Cardiol. *21*, 219–237.
2. Goldfarb, M.J., Saylor, M.A., Bozkurt, B., Code, J., Di Palo, K.E., Durante, A., Flanary, K., Masterson Creber, R., Ogunniyi, M.O., Rodriguez, F., et al. (2024). Patient-Centered Adult Cardiovascular Care: A Scientific Statement From the American Heart Association. Circulation *149*, e1176–e1188.
3. Richalet, J.P., Hermand, E., and Lhuissier, F.J. (2024). Cardiovascular Physiology and Pathophysiology at High Altitude. Nat. Rev. Cardiol. *21*, 75–88.
4. Wang, L., Qiu, S., Li, X., Zhang, Y., Huo, M., and Shi, J. (2023). Myocardial-Targeting Tannic Cerium Nanocatalyst Attenuates Ischemia/Reperfusion Injury. Angew. Chem. Int. Ed. Engl. *62*, e202305576.

5. Donahue, J.K., Chrispin, J., and Ajijola, O.A. (2024). Mechanism of Ventricular Tachycardia Occurring in Chronic Myocardial Infarction Scar. Circ. Res. *134*, 328–342.

6. González, A., López, B., Ravassa, S., San José, G., Latasa, I., Butler, J., and Díez, J. (2024). Myocardial Interstitial Fibrosis in Hypertensive Heart Disease: From Mechanisms to Clinical Management. Hypertension *81*, 218–228.

7. Zhang, X., Sun, Y., Yang, R., Liu, B., Liu, Y., Yang, J., and Liu, W. (2022). An Injectable Mitochondria-Targeted Nanodrug Loaded-Hydrogel for Restoring Mitochondrial Function and Hierarchically Attenuating Oxidative Stress to Reduce Myocardial Ischemia-Reperfusion Injury. Biomaterials *287*, 121656.

8. Wang, Y., Li, G., Yang, L., Luo, R., and Guo, G. (2022). Development of Innovative Biomaterials and Devices for the Treatment of Cardiovascular Diseases. Adv. Mater. *34*, e2201971.

9. Lee, J., Lee, S.G., Kim, B.S., Park, S., Sundaram, M.N., Kim, B.G., Kim, C.Y., and Hwang, N.S. (2024). Paintable Decellularized-ECM Hydrogel for Preventing Cardiac Tissue Damage. Adv. Sci. *11*, e2307353.

10. Lin, X., Liu, Y., Bai, A., Cai, H., Bai, Y., Jiang, W., Yang, H., Wang, X., Yang, L., Sun, N., and Gao, H. (2019). A Viscoelastic Adhesive Epicardial Patch for Treating Myocardial Infarction. Nat. Biomed. Eng. *3*, 632–643.

11. Boersma, E., Mercado, N., Poldermans, D., Gardien, M., Vos, J., and Simoons, M.L. (2003). Acute Myocardial Infarction. Lancet *361*, 847–858.

12. Gaudino, M., Sandner, S., An, K.R., Dimagli, A., Di Franco, A., Audisio, K., Harik, L., Perezgrovas-Olaria, R., Soletti, G., Fremes, S.E., et al. (2023). Graft Failure After Coronary Artery Bypass Grafting and its Association with Patient Characteristics and Clinical Events: A Pooled Individual Patient Data Analysis of Clinical Trials with Imaging Follow-Up. Circulation *148*, 1305–1315.

13. Tachibana, S., Yu, N.K., Li, R., Fernandez-Costa, C., Liang, A., Choi, J., Jung, D., Xiao, C., Kralli, A., Yates, J.R., et al. (2023). Perm1 Protects the Heart From Pressure Overload-Induced Dysfunction by Promoting Oxidative Metabolism. Circulation *147*, 916–919.

14. Hao, T., Li, J., Yao, F., Dong, D., Wang, Y., Yang, B., and Wang, C. (2017). Injectable Fullerenol/Alginate Hydrogel for Suppression of Oxidative Stress Damage in Brown Adipose-Derived Stem Cells and Cardiac Repair. ACS Nano *11*, 5474–5488.

15. Roshanbinfar, K., Vogt, L., Ruther, F., Roether, J.A., Boccaccini, A.R., and Engel, F.B. (2019). Nanofibrous Composite with Tailorable Electrical and Mechanical Properties for Cardiac Tissue Engineering. Adv. Funct. Mater. *30*, 1908612.

16. Zhou, Y., Liang, Q., Wu, X., Duan, S., Ge, C., Ye, H., Lu, J., Zhu, R., Chen, Y., Meng, F., and Yin, L. (2023). Sirna Delivery Against Myocardial Ischemia Reperfusion Injury Mediated by Reversibly Camouflaged Biomimetic Nanocomplexes. Adv. Mater. *35*, e2210691.

17. Schütte, J.P., Manke, M.C., Hemmen, K., Münzer, P., Schörg, B.F., Ramos, G.C., Pogoda, M., Dicenta, V., Hoffmann, S.H.L., Pinnecker, J., et al. (2023). Platelet-Derived Micrornas Regulate Cardiac Remodeling After Myocardial Ischemia. Circ. Res. *132*, 96–113.

18. Li, F., Liu, D., Liu, M., Ji, Q., Zhang, B., Mei, Q., Cheng, Y., and Zhou, S. (2022). Tregs Biomimetic Nanoparticle to Reprogram Inflammatory and Redox Microenvironment in Infarct Tissue to Treat Myocardial Ischemia Reperfusion Injury in Mice. J. Nanobiotechnol. *20*, 251.

19. Li, Q., Huang, Z., Wang, Q., Gao, J., Chen, J., Tan, H., Li, S., Wang, Z., Weng, X., Yang, H., et al. (2022). Targeted Immunomodulation Therapy for Cardiac Repair by Platelet Membrane Engineering Extracellular Vesicles Via Hitching Peripheral Monocytes. Biomaterials *284*, 121529.

20. Ali, H., Braga, L., and Giacca, M. (2020). Cardiac Regeneration and Remodelling of the Cardiomyocyte Cytoarchitecture. FEBS J. *287*, 417–438.

21. Niederer, S.A., Campbell, K.S., and Campbell, S.G. (2019). A Short History of the Development of Mathematical Models of Cardiac Mechanics. J. Mol. Cell. Cardiol. *127*, 11–19.

22. Shim, G., Breinyn, I.B., Martínez-Calvo, A., Rao, S., and Cohen, D.J. (2024). Bioelectric Stimulation Controls Tissue Shape and Size. Nat. Commun. *15*, 2938.

23. Suay-Corredera, C., and Alegre-Cebollada, J. (2022). The Mechanics of the Heart: Zooming in On Hypertrophic Cardiomyopathy and Cmybp-C. FEBS Lett. *596*, 703–746.

24. Puente, B.N., Kimura, W., Muralidhar, S.A., Moon, J., Amatruda, J.F., Phelps, K.L., Grinsfelder, D., Rothermel, B.A., Chen, R., Garcia, J.A., et al. (2014). The Oxygen-Rich Postnatal Environment Induces Cardiomyocyte Cell-Cycle Arrest through Dna Damage Response. Cell *157*, 565–579.

25. Boogerd, C.J., Perini, I., Kyriakopoulou, E., Han, S.J., La, P., van der Swaan, B., Berkhout, J.B., Versteeg, D., Monshouwer-Kloots, J., and van Rooij, E. (2023). Cardiomyocyte Proliferation Is Suppressed by Arid1a-Mediated Yap Inhibition During Cardiac Maturation. Nat. Commun. *14*, 4716.

26. de Abreu, R.C., Fernandes, H., da Costa Martins, P.A., Sahoo, S., Emanueli, C., and Ferreira, L. (2020). Native and Bioengineered Extracellular Vesicles for Cardiovascular Therapeutics. Nat. Rev. Cardiol. *17*, 685–697.

27. Yu, B., Li, H., Zhang, Z., Chen, P., Wang, L., Fan, X., Ning, X., Pan, Y., Zhou, F., Hu, X., et al. (2023). Extracellular Vesicles Engineering by Silicates-Activated Endothelial Progenitor Cells for Myocardial Infarction Treatment in Male Mice. Nat. Commun. *14*, 2094.

28. Park, H.J., Hoffman, J.R., Brown, M.E., Bheri, S., Brazhkina, O., Son, Y.H., and Davis, M.E. (2023). Knockdown of Deleterious Mirna in Progenitor Cell-Derived Small Extracellular Vesicles Enhances Tissue Repair in Myocardial Infarction. Sci. Adv. *9*, eabo4616.

29. Salazar-Puerta, A.I., Rincon-Benavides, M.A., Cuellar-Gaviria, T.Z., Aldana, J., Vasquez Martinez, G., Ortega-Pineda, L., Das, D., Dodd, D., Spencer, C.A., Deng, B., et al. (2023). Engineered Extracellular Vesicles Derived From Dermal Fibroblasts Attenuate Inflammation in a Murine Model of Acute Lung Injury. Adv. Mater. *35*, e2210579.

30. Jiang, J., Ni, L., Zhang, X., Wang, H., Liu, L., Wei, M., Li, G., and Bei, Y. (2023). Platelet Membrane-Fused Circulating Extracellular Vesicles Protect the Heart From Ischemia/Reperfusion Injury. Adv. Healthc. Mater. *12*, e2300052.

31. Tang, J., Cui, X., Zhang, Z., Xu, Y., Guo, J., Soliman, B.G., Lu, Y., Qin, Z., Wang, Q., Zhang, H., et al. (2022). Injection-Free Delivery of Msc-Derived Extracellular Vesicles for Myocardial Infarction Therapeutics. Adv. Healthc. Mater. *11*, e2100312.

32. Liu, X., Xiao, J., Zhu, H., Wei, X., Platt, C., Damilano, F., Xiao, C., Bezzerides, V., Boström, P., Che, L., et al. (2015). miR-222 Is Necessary for Exercise-Induced Cardiac Growth and Protects against Pathological Cardiac Remodeling. Cell Metab. *21*, 584–595.

33. Kang, J.Y., Kim, H., Mun, D., Yun, N., and Joung, B. (2021). Co-Delivery of Curcumin and Mirna-144-3P Using Heart-Targeted Extracellular Vesicles Enhances the Therapeutic Efficacy for Myocardial Infarction. J. Control. Release *331*, 62–73.

34. Aicher, A., Brenner, W., Zuhayra, M., Badorff, C., Massoudi, S., Assmus, B., Eckey, T., Henze, E., Zeiher, A.M., and Dimmeler, S. (2003). Assessment of the Tissue Distribution of Transplanted Human Endothelial Progenitor Cells by Radioactive Labeling. Circulation *107*, 2134–2139.

35. Seif-Naraghi, S.B., Singelyn, J.M., Salvatore, M.A., Osborn, K.G., Wang, J.J., Sampat, U., Kwan, O.L., Strachan, G.M., Wong, J., Schup-Magoffin, P.J., et al. (2013). Safety and Efficacy of An Injectable Extracellular Matrix Hydrogel for Treating Myocardial Infarction. Sci. Transl. Med. *5*, 173ra25.

36. Schlundt, C., Bietau, C., Klinghammer, L., Wiedemann, R., Rittger, H., Ludwig, J., and Achenbach, S. (2015). Comparison of Intracoronary Versus Intravenous Administration of Adenosine for Measurement of Coronary Fractional Flow Reserve. Circ. Cardiovasc. Interv. *8*, e001781.

37. Vogiatzidis, K., Zarogiannis, S.G., Aidonidis, I., Solenov, E.I., Molyvdas, P.A., Gourgoulianis, K.I., and Hatzoglou, C. (2015). Physiology of Pericardial Fluid Production and Drainage. Front. Physiol. *6*, 62.

38. Wang, L.L., Liu, Y., Chung, J.J., Wang, T., Gaffey, A.C., Lu, M., Cavanaugh, C.A., Zhou, S., Kanade, R., Atluri, P., et al. (2017). Local and Sustained Mirna Delivery From An Injectable Hydrogel Promotes Cardiomyocyte Proliferation and Functional Regeneration After Ischemic Injury. Nat. Biomed. Eng. *1*, 983–992.

39. Zhang, J., Zhu, W., Radisic, M., and Vunjak-Novakovic, G. (2018). Can We Engineer A Human Cardiac Patch for Therapy? Circ. Res. *123*, 244–265.

40. Zhu, D., Li, Z., Huang, K., Caranasos, T.G., Rossi, J.S., and Cheng, K. (2021). Minimally Invasive Delivery of Therapeutic Agents by Hydrogel Injection into the Pericardial Cavity for Cardiac Repair. Nat. Commun. *12*, 1412.

41. Fernandes, I., Funakoshi, S., Hamidzada, H., Epelman, S., and Keller, G. (2023). Modeling Cardiac Fibroblast Heterogeneity From Human Pluripotent Stem Cell-Derived Epicardial Cells. Nat. Commun. *14*, 8183.

42. Jiang, F., Yin, K., Wu, K., Zhang, M., Wang, S., Cheng, H., Zhou, Z., and Xiao, B. (2021). The Mechanosensitive Piezo1 Channel Mediates Heart Mechano-Chemo Transduction. Nat. Commun. *12*, 869.

43. Wei, X., Zhuang, L., Li, H., He, C., Wan, H., Hu, N., and Wang, P. (2020). Advances in Multidimensional Cardiac Biosensing Technologies: From Electrophysiology to Mechanical Motion and Contractile Force. Small *16*, e2005828.

44. Yokota, T., McCourt, J., Ma, F., Ren, S., Li, S., Kim, T.H., Kurmangaliyev, Y.Z., Nasiri, R., Ahadian, S., Nguyen, T., et al. (2020). Type V Collagen in Scar Tissue Regulates the Size of Scar After Heart Injury. Cell *182*, 545–562.e23.

45. Pesce, M., Duda, G.N., Forte, G., Girao, H., Raya, A., Roca-Cusachs, P., Sluijter, J.P.G., Tschöpe, C., and Van Linthout, S. (2023). Cardiac Fibroblasts and Mechanosensation in Heart Development, Health and Disease. Nat. Rev. Cardiol. *20*, 309–324.

46. Hill, M.C., Kadow, Z.A., Long, H., Morikawa, Y., Martin, T.J., Birks, E.J., Campbell, K.S., Nerbonne, J., Lavine, K., Wadhwa, L., et al. (2022). Integrated Multi-Omic Characterization of Congenital Heart Disease. Nature *608*, 181–191.

47. Liu, S., Li, K., Wagner Florencio, L., Tang, L., Heallen, T.R., Leach, J.P., Wang, Y., Grisanti, F., Willerson, J.T., Perin, E.C., et al. (2021). Gene Therapy Knockdown of Hippo Signaling Induces Cardiomyocyte Renewal in Pigs after Myocardial Infarction. Sci. Transl. Med. *13*, eabd6892.

48. Cheng, K., Shen, D., Smith, J., Galang, G., Sun, B., Zhang, J., and Marbán, E. (2012). Transplantation of Platelet Gel Spiked with Cardiosphere-Derived Cells Boosts Structural and Functional Benefits Relative to Gel Transplantation Alone in Rats with Myocardial Infarction. Biomaterials *33*, 2872–2879.

49. Ogle, B.M., Bursac, N., Domian, I., Huang, N.F., Menasché, P., Murry, C.E., Pruitt, B., Radisic, M., Wu, J.C., Wu, S.M., et al. (2016). Distilling Complexity to Advance Cardiac Tissue Engineering. Sci. Transl. Med. *8*, 342ps13.

50. Su, T., Huang, K., Ma, H., Liang, H., Dinh, P.U., Chen, J., Shen, D., Allen, T.A., Qiao, L., Li, Z., et al. (2019). Platelet-Inspired Nanocells for Targeted Heart Repair after Ischemia/Reperfusion Injury. Adv. Funct. Mater. *29*, 1803567.

51. Zhang, W., Hou, Y., Yin, S., Miao, Q., Lee, K., Zhou, X., and Wang, Y. (2024). Advanced Gene Nanocarriers/Scaffolds in Nonviral-Mediated Delivery System for Tissue Regeneration and Repair. J. Nanobiotechnol. *22*, 376.

52. Xie, Y., Ibrahim, A., Cheng, K., Wu, Z., Liang, W., Malliaras, K., Sun, B., Liu, W., Shen, D., Cheol Cho, H., et al. (2014). Importance of Cell-Cell Contact in the Therapeutic Benefits of Cardiosphere-Derived Cells. Stem Cell. *32*, 2397–2406.

53. Li, Z., Hu, S., Huang, K., Su, T., Cores, J., and Cheng, K. (2020). Targeted Anti-IL-1beta Platelet Microparticles for Cardiac Detoxing and Repair. Sci. Adv. *6*, eaay0589.

54. Montgomery, M., Ahadian, S., Davenport Huyer, L., Lo Rito, M., Civitarese, R.A., Vanderlaan, R.D., Wu, J., Reis, L.A., Momen, A., Akbari, S., et al. (2017). Flexible Shape-Memory Scaffold for Minimally Invasive Delivery of Functional Tissues. Nat. Mater. *16*, 1038–1046.

55. Mei, X., and Cheng, K. (2020). Recent Development in Therapeutic Cardiac Patches. Front. Cardiovasc. Med. *7*, 610364.

56. Tang, J., Vandergriff, A., Wang, Z., Hensley, M.T., Cores, J., Allen, T.A., Dinh, P.U., Zhang, J., Caranasos, T.G., and Cheng, K. (2017). A Regenerative Cardiac Patch Formed by Spray Painting of Biomaterials onto the Heart. Tissue Eng. Part C Methods *23*, 146–155.

57. Cheng, K., Malliaras, K., Shen, D., Tseliou, E., Ionta, V., Smith, J., Galang, G., Sun, B., Houde, C., and Marbán, E. (2012). Intramyocardial Injection of Platelet Gel Promotes Endogenous Repair and Augments Cardiac Function in Rats with Myocardial Infarction. J. Am. Coll. Cardiol. *59*, 256–264.

58. Spang, M.T., Middleton, R., Diaz, M., Hunter, J., Mesfin, J., Banka, A., Sullivan, H., Wang, R., Lazerson, T.S., Bhatia, S., et al. (2023). Intravascularly Infused Extracellular Matrix as a Biomaterial for Targeting and Treating Inflamed Tissues. Nat. Biomed. Eng. *7*, 94–109.

59. Contessotto, P., and Pandit, A. (2021). Therapies to Prevent Post-Infarction Remodelling: From Repair to Regeneration. Biomaterials *275*, 120906.

60. Kim, I.G., Hwang, M.P., Park, J.S., Kim, S.H., Kim, J.H., Kang, H.J., Subbiah, R., Ko, U.H., Shin, J.H., Kim, C.H., et al. (2019). Stretchable ECM Patch Enhances Stem Cell Delivery for Post-Mi Cardiovascular Repair. Adv. Healthc. Mater. *8*, e1900593.

61. Hegyi, B., Shimkunas, R., Jian, Z., Izu, L.T., Bers, D.M., and Chen-Izu, Y. (2021). Mechanoelectric Coupling and Arrhythmogenesis in Cardiomyocytes Contracting Under Mechanical Afterload in A 3D Viscoelastic Hydrogel. Proc. Natl. Acad. Sci. USA *118*, e2108484118.

62. Siti, H.N., Jalil, J., Asmadi, A.Y., and Kamisah, Y. (2022). Effects of Quercetin on Cardiac Function in Pressure Overload and Postischemic Cardiac Injury in Rodents: A Systematic Review and Meta-Analysis. Cardiovasc. Drugs Ther. *36*, 15–29.

63. Bui, A.L., Horwich, T.B., and Fonarow, G.C. (2011). Epidemiology and Risk Profile of Heart Failure. Nat. Rev. Cardiol. *8*, 30–41.

64. Nakamura, M., and Sadoshima, J. (2018). Mechanisms of Physiological and Pathological Cardiac Hypertrophy. Nat. Rev. Cardiol. *15*, 387–407.

65. Shen, D., Cheng, K., and Marbán, E. (2012). Dose-Dependent Functional Benefit of Human Cardiosphere Transplantation in Mice with Acute Myocardial Infarction. J. Cell Mol. Med. *16*, 2112–2116.

66. Li, Z., Hu, S., and Cheng, K. (2019). Chemical Engineering of Cell Therapy for Heart Diseases. Acc. Chem. Res. *52*, 1687–1696.

67. Vandergriff, A.C., Hensley, M.T., and Cheng, K. (2015). Isolation and Cryopreservation of Neonatal Rat Cardiomyocytes. J. Vis. Exp. *9*, 52726.

68. Adapala, R.K., Katari, V., Kanugula, A.K., Ohanyan, V., Paruchuri, S., and Thodeti, C.K. (2023). Deletion of Endothelial Trpv4 Protects Heart From Pressure Overload-Induced Hypertrophy. Hypertension *80*, 2345–2356.

69. Sun, X., Chen, H., Gao, R., Qu, Y., Huang, Y., Zhang, N., Hu, S., Fan, F., Zou, Y., Hu, K., et al. (2023). Intravenous Transplantation of An Ischemic-Specific Peptide-Tpp-Mitochondrial Compound Alleviates Myocardial Ischemic Reperfusion Injury. ACS Nano *17*, 896–909.

70. Lyu, Q., Gong, S., Lees, J.G., Yin, J., Yap, L.W., Kong, A.M., Shi, Q., Fu, R., Zhu, Q., Dyer, A., et al. (2022). A Soft and Ultrasensitive Force Sensing Diaphragm for Probing Cardiac Organoids Instantaneously and Wirelessly. Nat. Commun. *13*, 7259.

71. Wang, Y., Tong, X., Shi, X., Keswani, T., Chatterjee, E., Chen, L., Li, G., Lee, K., Guo, T., and Yu, Y. (2023). Chiral Cell Nanomechanics Originated in Clockwise/Counterclockwise Biofunctional Microarrays to Govern the Nuclear Mechanotransduction of Mesenchymal Stem Cells. ACS Appl. Mater. Interfaces *15*, 48038–48049.

72. Kechagia, J.Z., Ivaska, J., and Roca-Cusachs, P. (2019). Integrins as Biomechanical Sensors of the Microenvironment. Nat. Rev. Mol. Cell Biol. *20*, 457–473.

73. Pang, X., He, X., Qiu, Z., Zhang, H., Xie, R., Liu, Z., Gu, Y., Zhao, N., Xiang, Q., and Cui, Y. (2023). Targeting Integrin Pathways: Mechanisms and Advances in Therapy. Signal Transduct. Target. Ther. *8*, 1.

74. Sleeboom, J.J.F., van Tienderen, G.S., Schenke-Layland, K., van der Laan, L.J.W., Khalil, A.A., and Verstegen, M.M.A. (2024). The Extracellular Matrix as Hallmark of Cancer and Metastasis: From Biomechanics to Therapeutic Targets. Sci. Transl. Med. *16*, eadg3840.

75. Li, X., Combs, J.D., 3rd, Salaita, K., and Shu, X. (2023). Polarized Focal Adhesion Kinase Activity within a Focal Adhesion During Cell Migration. Nat. Chem. Biol. *19*, 1458–1468.

76. Wang, Y., Chatterjee, E., Li, G., Xu, J., and Xiao, J. (2024). Force-Sensing Protein Expression in Response to Cardiovascular Mechanotransduction. EBioMedicine *110*, 105412.

77. Liu, L., Zhao, Q., Kong, M., Mao, L., Yang, Y., and Xu, Y. (2022). Myocardin-Related Transcription Factor a Regulates Integrin Beta 2 Transcription to Promote Macrophage Infiltration and Cardiac Hypertrophy in Mice. Cardiovasc. Res. *118*, 844–858.

78. Zhang, Y., Su, S.A., Li, W., Ma, Y., Shen, J., Wang, Y., Shen, Y., Chen, J., Ji, Y., Xie, Y., et al. (2021). Piezo1-Mediated Mechanotransduction Promotes Cardiac Hypertrophy by Impairing Calcium Homeostasis to Activate Calpain/Calcineurin Signaling. Hypertension *78*, 647–660.

79. Ke, W., Liao, Z., Liang, H., Tong, B., Song, Y., Li, G., Ma, L., Wang, K., Feng, X., Li, S., et al. (2023). Stiff Substrate Induces Nucleus Pulposus Cell Ferroptosis Via Yap and N-Cadherin Mediated Mechanotransduction. Adv. Healthc. Mater. *12*, e2300458.

80. Lu, T., Zhang, J., Cai, J., Xiao, J., Sui, X., Yuan, X., Li, R., Li, Y., Yao, J., Lv, G., et al. (2022). Extracellular Vesicles Derived From Mesenchymal Stromal Cells as Nanotherapeutics for Liver Ischaemia-Reperfusion Injury by Transferring Mitochondria to Modulate the Formation of Neutrophil Extracellular Traps. Biomaterials *284*, 121486.

81. Zhang, K., and Cheng, K. (2023). Stem Cell-Derived Exosome versus Stem Cell Therapy. Nat. Rev. Bioeng. *1*, 608–609.

82. Li, Y., Chen, X., Jin, R., Chen, L., Dang, M., Cao, H., Dong, Y., Cai, B., Bai, G., Gooding, J.J., et al. (2021). Injectable Hydrogel with Msns/Microrna-21-5P Delivery Enables Both Immunomodification and Enhanced Angiogenesis for Myocardial Infarction Therapy in Pigs. Sci. Adv. *7*, eabd6740.

83. Cao, Y., Bojjireddy, N., Kim, M., Li, T., Zhai, P., Nagarajan, N., Sadoshima, J., Palmiter, R.D., and Tian, R. (2017). Activation of γ2-AMPK Auppresses Ribosome Biogenesis and Protects against Myocardial Ischemia/Reperfusion Injury. Circ. Res. *121*, 1182–1191.

84. Subramani, J., Kundumani-Sridharan, V., and Das, K.C. (2021). Chaperone-Mediated Autophagy of eNOS in Myocardial Ischemia-Reperfusion Injury. Circ. Res. *129*, 930–945.

85. Gao, R., Wang, L., Bei, Y., Wu, X., Wang, J., Zhou, Q., Tao, L., Das, S., Li, X., and Xiao, J. (2021). Long Noncoding RNA Cardiac Physiological Hypertrophy-Associated Regulator Induces Cardiac Physiological Hypertrophy and Promotes Functional Recovery after Myocardial Ischemia Reperfusion Injury. Circulation *144*, 303–317.

STAR★METHODS

KEY RESOURCES TABLE

REAGENT or RESOURCE	SOURCE	IDENTIFIER
Antibodies		
Bax Rabbit pAb	ABclonal	Cat#A19684, RRID: AB_2862733
Bcl-2 Rabbit pAb	Affinity Biosciences	Cat # AF6139, RRID: AB_2835021
[KO Validated] Caspase3 Rabbit pAb	ABclonal	Cat #A2156, RRID: AB_2862975
COL1A2 (S3) Polyclonal Antibody	Bioworld	Cat #BS1530, RRID: AB_1662101
α-Smooth Muscle Actin (ACTA2) Rabbit mAb	ABclonal	Cat #A17910, RRID: AB_2861755
CD63 Rabbit pAb	ABclonal	Cat # A5271, RRID: AB_2766092
TSG101/VPS23 Rabbit pAb	ABclonal	Cat # A1692, RRID: AB_2763744
Alix (1A12) Antibody	Santa Cruz Biotechnology	Cat # sc-53540, RRID: AB_673819
CD9 Rabbit mAb	ABclonal	Cat # A19027, RRID: AB_2862519
β-actin Rabbit mAb	ABclonal	Cat #AC004, RRID: AB_2737399
Monoclonal Anti-alpha-Actinin (Sarcomeric) Antibody produced in mouse	Sigma-Aldrich	Cat #A7811, RRID: AB_476766)
Cy3-AffiniPure Donkey Anti-Mouse IgG (H + L)	Jackson ImmunoResearch Labs	Cat #715-165-151, RRID: AB_2315777
Alexa Fluor 488-AffiniPure Goat Anti-Mouse IgG (H + L)	Jackson ImmunoResearch Labs	Cat #115-545-003, RRID: AB_2338840
Integrin-β1/CD29 Rabbit mAb	ABclonal	Cat #A2217, AB_2764232
Vinculin Rabbit mAb	ABclonal	Cat #A2752, RRID: AB_2863020
TLN1 Rabbit pAb	ABclonal	Cat #A4158, RRID: AB_2765532
FAM38A/PIEZO1 Rabbit mAb	ABclonal	Cat #A23380, RRID: AB_3095404
MYH9 Polyclonal Antibody	Proteintech	Cat # 11128-1-AP, RRID: AB_2147294
YAP1 Rabbit mAb	ABclonal	Cat #A19134, RRID: AB_2862627
HMBOX1 Polyclonal Antibody	Proteintech	Cat #16123-1-AP, RRID: AB_10794445
HIPK1 Polyclonal Antibody	Thermo Fisher Scientific	Cat# PA5-115358, RRID:AB_2899994
HIPK2 Polyclonal Antibody	Abcam	Cat #ab108543, RRID: AB_10860868
Chemicals, peptides, and recombinant proteins		
Hoechst 33342	KeyGEN BioTECH	Cat #KGA212-1
DiD (1,1′-Dioctadecyl-3,3,3′,3′-Tetramethylindodicarbocyanine, 4-Chlorobenzenesulfonate Salt)	Beyotime	Cat #C1039
A-Type Gelatin Powder	Sigma Aldrich	Cat #9000-70-8
Methacrylic Anhydride (MAA)	Sigma Aldrich	Cat #760-93-0
Ischemia-Targeting Polypeptide	QYAOBIO	N/A
Critical commercial assays		
Western Blot Lysis Buffer	KeyGEN BioTECH	Cat #KGP701-100
TaKaRa BCA Protein Assay Kit	Takara	Cat #T9300A
Masson's Trichrome Staining Kit	Solarbio	Cat #G1340
H&E Staining Kit	KeyGEN BioTECH	Cat #KGA224
TUNEL FITC Apoptosis Detection Kit	Vazyme	Cat #A111-03
Tanon™ High-sig ECL Western Blotting Substrate	Tanon	Cat #180-501
Cell Counting Kit-8	Dojindo	Cat #CK04
Cytotoxicity Detection KitPLUS	Roche	Cat#11644793001
RevertAid First Strand cDNA Synthesis Kit	Thermo Fisher Scientific	Cat#K1622
TaKaRa SYBR Premix Ex Taq (Tli RBaseH Plus)	Takara	Cat#RR420A

(*Continued on next page*)

Continued		
REAGENT or RESOURCE	SOURCE	IDENTIFIER
Deposited data		
^{1}H-NMR data	Protein DataBank	Gelatin BMRB ID: 26354 GelMA BMRB ID: 26355
Experimental models: Organisms/strains		
C57BL/6 Aged Mice (SPF)	Zhejiang Weitong Lihua Experimental Animal Technology Co., Ltd.	N/A
Oligonucleotides		
rno-miR-222 mimics sequence: AGCUACAUCUGGCUACUGGGU	RIBOBIO	N/A
mmu-miR-222 mimics sequence: AGCUACAUCUGGCUACUGGGUCU	RIBOBIO	N/A
Software and algorithms		
ImageJ	ImageJ	https://imagej.nih.gov/ij/
GraphPad Prism 8.0 Software	GraphPad	https://www.graphpad.com/scientific-software/prism/www.graphpad.com/scientific-software/prism/
Origin 9.0	Origin	https://www.originlab.com/

EXPERIMENTAL MODEL AND STUDY PARTICIPANT DETAILS

Male C57BL/6 mice (8 weeks old, sourced from Zhejiang Weitong Lihua Experimental Animal Technology Co., Ltd., China) were used to establish myocardial IRI by ligating the left anterior descending (LAD) coronary artery for 0.5 h.[83–85] Subsequently, the LAD-ligated mice underwent reperfusion for either 24 h or 3 weeks, to model acute or chronic IRI, respectively. To mitigate cardiac reperfusion damage, mice were randomly allocated into four groups: PBS control, GelMA in PBS (GEL), targeting miR-222-engineered EVs (TeEV), and TeEV-loaded GEL (GEL-TeEV). Each mouse received a 20 μL intrapericardial injection of PBS or GEL hydrogel, with or without 1×10^{9} therapeutics (eEVs or TeEVs), followed by exposure to 405 nm light for 30 s. The concentration of the therapeutics (eEVs or TeEVs) was fixed to be 5×10^{10} particles/mL. Additionally, 20 μL of PBS solution was injected in a similar manner into the sham group. All animal experiments were approved by the Committee of Animal Ethics at Shanghai University.

METHOD DETAILS

Chemical synthesis of viscoelastic GEL precursors

Viscoelastic GEL precursors were designed and synthesized by introducing methacryloyl groups into gelatin chains. In brief, 10 g A-type gelatin powder (Sigma Aldrich, USA) was completely dissolved in 90 mL phosphate buffered saline (PBS, pH = 7.6 by 1 N sodium hydroxide solution) and stirred under 400 rpm at 50°C to obtain a homogeneous gelatin aqueous solution. Afterward, 2 mL of methacrylic anhydride (MAA, Sigma-Aldrich, USA) was slowly added to the gelatin solution at a dropping rate of 0.5 mL/min under 400 rpm, stirring at 50°C to synthesize GEL precursors. The reaction mixture was stirred in the dark for 3 h and then diluted in 5-folds with PBS at 50°C. The diluted solution was dialyzed against ultrapure water for 5 days using dialysis tubing with a cellulose membrane (14 kD molecular weight cut-off, Spectrum Laboratories, USA). The ultrapure water was replaced three times per day to remove residual MA monomers. The GEL precursor solution was filtered with 0.22 μm filters for sterilization and then lyophilized for 3 days to obtain porous GEL sponges, which were stored at −20°C for further use.

^{1}H nuclear magnetic resonance (^{1}H-NMR) analysis

^{1}H-NMR spectroscopy was used to quantify the content of methacryloyl groups in gelatin chains. The ^{1}H-NMR spectra were obtained using 300 MHz single-axis gradient inverse probe on an NMR AL300 spectrometer (JEOL, Japan). Fifteen milligrams of GEL precursors were dissolved in 0.5 mL of deuterium oxide (D_2O), containing 0.05 wt % 3-(trimethylsilyl)propionic-2,2,3,3-d4 acid sodium salt for calibration (Sigma-Aldrich, USA). Non-functionalized gelatin was also measured and analyzed for comparison.

Cell culture and targeting miR-222-engineered EV construction

Human umbilical cord mesenchymal stem cells (HUC-MSCs) were cultured in Hyclone MEM Alpha Modification (SH30265.01, Hyclone, USA) with EV-removed UltraGRO GMP grade (HPCPLCGL50, Helios Bioscience, USA) in a 37°C and 5% CO_2 incubator. The supernatant of HUC-MSCs was collected to obtain the EVs by a 4-step differential centrifugation enrichment method in an Optima XPN-100 Ultracentrifuge (BECKMAN COULTER): (1) Centrifugation at 300*g* at 4°C for 10 min to collect supernatant; (2) centrifugation

at 2,000 g at 4°C for 10 min to collect supernatant; (3) centrifugation at 10,000 g at 4°C for 30 min to collect supernatant; and (4) centrifugation at 100,000 g at 4°C for 70 min to collect the deposition. The deposited EVs were obtained for further experiments. The miR-222 mimics (RiboBio, China) were transformed into HUC-MSC-derived EVs to establish miR-222-engineered EVs (eEV) by electroporation method. In addition, the ischemia-targeting polypeptide (coded with a sequence of Cys-Ser-Thr-Ser-Met-Leu-Lys-Ala-Cys) (QYAOBIO, China) was bonded to miR-222-engineered EVs to form ischemia-targeting miR-222-engineered EVs (TeEV). The sequence of miR-222 mimics are as follows: mmu-miR-222-AGCUACAUCUGGCUACUGGGUCU [Mus musculus (mmu)], rno-miR-222-AGCUACAUCUGGCUACUGGGU [Rattus norvegicus (rno)].

Transmission electron microscope (TEM)

The targeting engineered EVs (4×10^9 particles/mL) were characterized by TEM (TECNAI G2 F20, USA) to observe their geometrical morphology. 10 μL of EV suspension was dropped onto 200-mesh copper grids with carbon-based modification. After 5-min incubation, excessive liquid was removed by filter paper and EVs were stained with uranium dioxide acetate and then dried to capture images by TEM. The targeting engineered EVs (8×10^7 particles/mL) were measured by nanoparticle tracking analysis (NTA, ZetaView, Particle Metrix, Germany) to calculate the physical sizes and average particle sizes of eEVs and TeEVs.

GEL-based hydrogel fabrication

GEL hydrogel was fabricated through photo-crosslinking by incorporating GEL precursor and photoinitiator. Specifically, 10 wt % GEL precursor and 0.5% photoinitiator (LAP 405 nm) were homogenously dissolved in sterilized PBS, with or without TeEVs. GEL with TeEV was defined as GEL-TeEV. A 20 μL aliquot of hydrogel solution, loaded with 1×10^9 TeEVs, was injected into the impaired cardiac region and crosslinked under 405 nm UV light for 20 s to form a cardiac TeEV-loaded patch.

Observation of hydrogel morphology

The morphology of GEL hydrogel samples, with or without TeEVs, was observed using a scanning electron microscope (SEM, GeminiSEM 300 ZEISS, Germany). The hydrogels were immediately immersed in liquid nitrogen, freeze-dried, and then imaged by SEM to examine the GEL microstructures. To prevent electron aggregation on the hydrogel surface, the samples underwent gold sputtering. The acceleration voltage was set at 5 kV.

Mechanical measurement of stiffness and adhesive force

The Mechanical properties of GEL, cardiac tissues, and cells were assessed using an atomic force microscope (MFP-3D-Bio AFM, Asylum Research, USA) within a nanoindentation system. GEL hydrogels, with or without TeEVs, were maintained in PBS for 24 h. Prior to AFM analysis, a self-contained optical microscope was used to define the localization of the AFM probe. A Si_3N_4 cantilever (Novascan Technologies Inc., USA) with a 600 nm glass ball and a nominal spring constant of 0.06 N/m was employed in our experiments. Spring constants were verified through a thermal noise protocol. Measurements were taken at an indentation speed of 4 μm/s and a trigger force of 2 nN. Force-distance curves were obtained to evaluate the hydrogel's stiffness and adhesive force. For cell experiments, cardiomyocytes cultured on cell culture plates were measured within 2 h to ensure viability. A linear fitting operation adjusted the baseline for each curve according to a Hertz contact model.

Equilibrium absorption ratio

The water absorption and infiltration capabilities of GEL hydrogels were assessed through the equilibrium absorption ratio. Hydrogels, with or without TeEVs, were shaped into 8 mm diameter and 2 mm height discs, then immersed in PBS within a 37°C and 5% CO_2 incubator for 24 h. The wet weight (W_{wet}) was determined post immersion and drying on filter paper, and compared to the dry weight (W_{dry}) after freeze-drying. The absorption ratio was calculated using the equation: $W_{wet}/W_{dry}\times100\%$.

Weight loss of hydrogel by enzymatic degradation

The stability of GEL hydrogels, with or without TeEVs, was evaluated under enzymatic degradation conditions. The hydrogel samples were cut into discs with a diameter of 8 mm and a height of 2 mm, and then swollen in PBS for 24 h to reach absorption equilibrium. Subsequently, these discs were immersed in 2 mL of PBS supplemented with 10 units/mL collagenase (Clostridium Hhistolyticum, USA) and agitated at 60 rpm within a 37°C and 5% CO_2 incubator. At specific intervals (1, 2, 4, 8, 16, and 32 h), the hydrogel samples were retrieved, the residual buffer was removed with filter paper, and they were weighed. The degree of degradation (η_Δ) was calculated using the equation: $\eta_\Delta=(1- W_{residual}/W_{initial})\times100\%$, where $W_{initial}$ and $W_{residual}$ are the initial and residual wet weights, respectively.

TeEV release profile in GEL

GEL precursors with or without TeEVs (5×10^{10} particles/mL), were placed in cell plates and cured using 405 nm light. After curing, PBS was added to each well to commence the EV release experiment. Over various time points (0, 6, 12, 24, 48, and 72 h) PBS was collected to measure the released TeEV amounts using NTA. The release capacity was quantified by the ratio of released TeEV amount to the total TeEVs in the GEL.

Cellular internalization of TeEVs in neonatal rat cardiomyocytes

Prior to cellular internalization, an oxygen-glucose deprivation reperfusion (OGDR) model was established in NRCMs. The cells were cultured in DMEM medium supplemented with 10% horse serum and 5% FBS. NRCMs were initially cultured in glucose-free and serum-free DMEM under anoxic conditions at 37°C for 8 h, followed by 12 h in a normoxic environment with glucose and serum. Subsequently, the OGDR-treated NRCMs were incubated in 8-well microslides (Ibidi GmbH, Germany) with 1×10^4 cells per well. DiD-labeled eEVs and TeEVs were added to the wells to study cellular uptake over 4 h. The cells were then fixed with 4% cold paraformaldehyde (PFA) for 10 min. Fixed cells were incubated with α-actinin primary antibody at 4°C overnight, followed by Alexa Fluor 488 secondary antibody. After washing with PBS, nuclei were stained with Hoechst 33342. Cellular uptake of DiD-labeled EVs was observed using a laser confocal scanning microscope (FV3000, Olympus, Japan) and further quantified by flow cytometry. Both control and OGDR-stressed NRCMs were cultured in 12-well plates (2.5×10^4 cells/cm^2) and incubated with either PBS, DiD-labeled eEVs, or DiD-labeled TeEVs for 4 h. The normalized fluorescence density was examined and quantified by CytoFlex (Beckman Coulter, China).

Cell viability assay

Cell viability was assessed using a Cell Counting Kit-8 (CK04, Dojindo, Japan). NRCMs were seeded in 96-well plates with different conditions: PBS, GEL, TeEV, GEL-TeEV. The cells were cultured for 24, 48, and 72 h. NRCMs were cultured atop GEL and GEL-TeEVs to simulate *in vitro* interaction between GEL hydrogels and cardiomyocytes.

Tunel staining and apoptosis analysis of NRCMs

Prior to cell seeding, 12-well plates were coated with gel and GEL-TeEV and cured under UV light. Post-curing, NRCMs with or without OGDR treatment were cultured in the coated plates in a 37°C and 5% CO_2 incubator for 12 h. Cells were fixed with 4% cold PFA for 10 min and permeabilized with 1% Triton X-100 for 10 min. Tunel staining was performed using a FITC detection kit (A111-03, Vazyme) following the manufacturer's protocols to assess apoptosis. Western Blot (WB) assays were conducted to evaluate the expression of apoptosis-related proteins using Bax Rabbit pAb (Abclonal, A19684), Bcl2 Rabbit pAb (Affinity Biosciences, AF6139), with β-Actin (AC004, Abclonal) as a loading control.

Intrapericardial injection

The mice were anesthetized with 2% isoflurane. The animals were placed on a heating pad to maintain body temperature at 37°C with a supine position and a ventilator was used to acquire passive respiration. After 0.5-h myocardial ischemia, the therapeutic was injected into the pericardial cavity with a micro-syringe and GEL was instantly cured under UV crosslinking. After intrapericardial injection, the surgical incision was sutured and the animals were fed for IRI repair assay.

2,3,5-Triphenyl tetrazolium chloride (TTC) staining

Post 24-h reperfusion, under the acute IRI model, TTC staining was performed to evaluate cardiac infarct size and area. 1% Evans blue in PBS was injected into the left ventricle (LV) of the injured heart, followed by sectioning the hearts into 1 mm thick slices, which were then stained with TTC reagent. The area at risk relative to LV weight (AAR/LV) was examined to confirm the successful induction of the IRI model. Infarct size was quantified using the ratio of infarct size to AAR (INF/AAR).

Myocardial apoptosis evaluation

Frozen heart slices, 10-μm-thick, were fixed with 4% cold PFA for 10 min and washed thrice with PBS. The samples were then stained using G3250 DeadEnd Fluorometric Tunel System following the manufacturer's protocols. Cardiomyocytes were incubated overnight with α-actinin primary antibody and subsequently stained with Cy3 dye for 1 h. Nuclei were counterstained with Hoechst 33342 for 10 min in the dark. Stained cells were visualized using a laser confocal microscope (Olympus, FV3000) to capture fluorescent images. WB assays quantified the expression levels of apoptosis-related proteins (Bax, Bcl2, Caspase3, and cleaved Caspase3).

Lactate dehydrogenase (LDH) assay

Serum LDH levels were measured using a Cytotoxicity Detection KitPLUS (11644793001, Roche, Switzerland). Absorbance at 492 nm was recorded using an ELISA reader (SpectraMax iD3, Molecular Devices) to compare LDH levels across different treatment groups.

Hematoxylin & eosin (H&E) and masson's trichrome staining

Post-collection, tissues (heart, liver, spleen, lung, and kidney) were fixed in 4% neutral buffered formalin, dehydrated and embedded in paraffin. Tissue sections of 5-μm thickness were cut for histological analysis. For H&E staining, sections were deparaffinized and stained using KeyGEN BioTECH's kit (KGA224, China). Masson's trichrome staining was performed with Solarbio's kit (G1340) to assess cardiac fibrosis. Stained sections were imaged using an optical microscope and analyzed with ImageJ software.

Heart function analysis

Mice were treated with intrapericardial injections of 20 μL of PBS, GEL, TeEV, or GEL-TeEV post-IRI. After 3 weeks in the chronic IRI model, cardiac function was assessed using a Vevo2100 echocardiometer (FUJIFILM Visual Sonics) to measure left ventricle shortening fraction (FS) and ejection fraction (EF).

Real-time quantitative PCR (RT-qPCR)

Total RNA was extracted from mouse heart tissues using the TRIzol RNA Plus Kit (Takara, Japan). Total RNA from EVs was isolated by miRNeasy Mini Kit (HB-1277, QIAGEN, Germany). RNA was reverse transcribed to complementary DNA (cDNA) using the RevertAid First Strand cDNA Synthesis Kit (K1622, Thermo Fisher Scientific., USA). mRNA expression levels were quantitatively analyzed using the Roche LightCycleer480 PCR system and a Takara SYBR Premix Ex Taq (Tli RBaseH Plus). The internal control was 18S rRNA. The primers were used for qPCR in Table S1. For the measurement of miR-222 levels, the reverse transcription primers and the RT-qPCR primers of miR-222 and U6 (internal control) were purchased from RiboBio, China.

Mechanical signaling analysis of adhesion proteins, cytoskeleton and YAP

Frozen heart tissue slices, 10 μm in thickness, were fixed with 4% cold PFA for 10 min. Blocking was performed with BSA for 1 h, followed by three PBS washes. Samples were incubated overnight with primary antibodies against Integrin (Integrin-β1/CD29 Rabbit mAb, A2217, ABclonal, China), vinculin (Vinculin Rabbit mAb, A2752, ABclonal, China), Talin-1 (TLN1 Rabbit pAb, A4158, ABclonal, China), Piezo1 (FAM38A/PIEZO1 Rabbit mAb, A23380, ABclonal, China), Myosin (MYH9 Polyclonal Antibody, 11128-1-AP, Proteintech, China), YAP (YAP1 Rabbit mAb, A19134, ABclonal, China). Following primary antibody incubation, appropriate secondary antibodies were applied for immunofluorescence (IF) staining. The same primary antibodies were utilized for WB analysis to further evaluate protein expression levels.

QUANTIFICATION AND STATISTICAL ANALYSIS

Data were expressed as mean ± standard deviation (SD). The significance of differences between two groups was assessed using the unpaired Student's t test, while comparisons among four or more groups were performed using one-way ANOVA test followed by Bonferroni test via GraphPad 8.0 (GraphPad, USA). two-way ANOVA test followed by Tukey post hoc test was used to analyze two variables. A p-value of less than 0.05 was considered statistically significant.